International Journal of Biological Macromolecules 383 (2026) 154646

Contents lists available at ScienceDirect

International Journal of Biological Macromolecules

journal homepage: www.elsevier.com/locate/ijbiomac

Carbohydrate functionalization modulates the mucosal transport and immunological activity of chitosan nanoparticles

Mariana Colaço [a,b,c], João Panão-Costa [a,b,c], Elena Del Favero [f], Caterina Ricci [f], Virginia Patterlini [d], Giulia Climani [d], Ilaria Ferraboschi [h], Cristina Sissa [h], Filipa Lebre [g], Ernesto Alfaro-Moreno [g], Fabio Sonvico [d,e], Olga Borges [a,b,c,*]

[a] CNC-UC - Center for Neuroscience and Cell Biology, University of Coimbra, Portugal
[b] CIBB - Center for Innovative Biomedicine and Biotechnology, University of Coimbra, Portugal
[c] Department of Pharmaceutical Technology, Faculty of Pharmacy, University of Coimbra, Portugal
[d] Department of Food and Drug Science, ADDRes-Advanced Drug Delivery Research Lab, University of Parma, Parma, Italy
[e] Interdepartmental Research Center for the Innovation of Health Products Biopharmanet-TEC, University of Parma, Parma, Italy
[f] Department of Medical Biotechnologies and Translational Medicine, LITA, University of Milan, Milan, Italy
[g] Nanosafety Group, International Iberian Nanotechnology Laboratory, Braga, Portugal
[h] Department of Chemistry, Life Sciences and Environmental Sustainability, University of Parma, Parma, Italy

ARTICLE INFO

Keywords:
Carbohydrate-functionalized chitosan nanoparticles
Glycoengineering
Nasal epithelial permeability

ABSTRACT

Mucosal vaccination represents an attractive strategy for preventing respiratory infections by establishing immune protection at the site of pathogen entry. However, the development of intranasal vaccines remains challenging due to limited epithelial transport, rapid mucociliary clearance, and the tolerogenic nature of the mucosal immune environment. Here, we report glycoengineered chitosan nanoparticles (NPs) functionalized with lactobionic acid, gluconic acid, and mannose as a platform to enhance mucosal vaccine delivery and immune activation. Carbohydrate functionalization preserved the mucoadhesive properties of chitosan while improving nanoparticle transport across the nasal epithelium, as demonstrated in human nasal epithelial models and confirmed *ex vivo* using rabbit nasal tissue. Mechanistic studies revealed receptor-mediated uptake of functionalized NPs by human macrophages, resulting in cellular internalization and polarization toward a pro-inflammatory M1 phenotype. Among the formulations evaluated, mannosylated NPs demonstrated a particularly pronounced immunostimulatory profile and promoted robust antigen-specific mucosal and systemic immune responses following intranasal administration, including elevated secretory IgA production, T-cell memory differentiation, and a balanced Th1/Th2/Th17 cytokine profile. Collectively, these findings demonstrate that glycoengineering of chitosan nanoparticles enhances both epithelial transport and immune activation through targeted nano–bio interactions. This work establishes carbohydrate-functionalized chitosan nanocarriers as a platform for effective intranasal vaccines against respiratory pathogens, including SARS-CoV-2.

1. Introduction

Vaccination has proven to be one of the most effective strategies for controlling viral pandemics. While multiple platforms have been developed for SARS-CoV-2 vaccination, including mRNA-based, DNA-based, viral vector, and protein subunit vaccines, significant limitations remain in achieving durable protection at the site of viral entry [1]. Protein subunit vaccines are particularly attractive due to their safety, stability, and scalability; however, their clinical performance is often limited by weak intrinsic immunogenicity, requiring effective adjuvant and delivery systems to achieve robust immune activation.

A key limitation of current vaccination strategies is the insufficient induction of mucosal immunity in the respiratory tract. Most licensed vaccines are administered intramuscularly and primarily induce systemic IgG responses, with limited stimulation of secretory IgA (sIgA) and local immune defenses at mucosal surfaces [2]. Since respiratory viruses initiate infection at mucosal barriers, the absence of strong local immunity contributes to continued viral transmission even in vaccinated

* Corresponding author at: CNC-UC - Center for Neuroscience and Cell Biology, University of Coimbra, Portugal.
E-mail address: oborges@ff.uc.pt (O. Borges).

https://doi.org/10.1016/j.ijbiomac.2026.154646
Received 9 July 2026; Received in revised form 22 September 2026; Accepted 25 September 2026
Available online 26 September 2026
0141-8130/© 2026 The Authors. Published by Elsevier B.V. This is an open access article under the CC BY-NC license (http://creativecommons.org/licenses/by-nc/4.0/).

populations. This highlights a critical need for vaccine strategies capable of inducing both systemic and mucosal immune responses.

Intranasal vaccination represents a promising approach to address this limitation, as it directly targets the respiratory mucosa and can promote local sIgA production and tissue-resident immune responses [3]. However, despite its theoretical advantages, intranasal immunization remains challenging due to several physiological and biochemical barriers. The nasal cavity is protected by a mucus layer composed of highly glycosylated mucins, antimicrobial proteins, and enzymes, which together form a dense and dynamic barrier that limits antigen diffusion. In addition, mucociliary clearance continuously removes foreign particles from the nasal surface, significantly reducing antigen residence time and limiting uptake by immune cells. Furthermore, the nasal environment is inherently tolerogenic, which can further reduce antigen-induced immune activation.

Consistent with this rationale, several intranasal vaccine strategies have been explored for SARS-CoV-2, including viral vector, live attenuated and protein subunit approaches, with promising mucosal immune responses reported in preclinical studies [4,5]. For protein subunit-based intranasal vaccines, delivery systems have predominantly relied on lipid- and emulsion-based formulations to enhance antigen stability and mucosal immunogenicity, including oil-in-water emulsions and cationic liposomal formulations incorporating immunostimulatory molecules [6,7]. However, these platforms largely rely on passive diffusion and nonspecific uptake, limiting their interaction with antigen-presenting cells (APCs) in nasal-associated lymphoid tissue (NALT) and resulting in suboptimal antigen retention and variable mucosal immune responses. In this setting, mucoadhesive polymeric nanocarriers offer a promising alternative, as they prolong residence time at the nasal mucosa while enabling surface functionalization for improved mucus penetration and more selective uptake by APCs.

Chitosan, a cationic biopolymer derived from the abundant marine polysaccharide chitin, offers a promising solution for overcoming the challenges associated with nasal antigen delivery. This naturally occurring polymer exhibits desirable biocompatibility and mucoadhesive properties, enabling it to form robust interactions with the negatively charged components of the mucosal surface. Upon interaction with mucus, chitosan forms gel-like structures that enhance antigen retention and improve contact with the absorption site [8]. In addition, chitosan can transiently open epithelial tight junctions, facilitating antigen transport across the nasal barrier. Chitosan's versatility extends to its modification, where its hydroxyl and amine groups can be easily altered to fine-tune its surface properties, such as hydrophilicity and charge, without the need for harsh synthetic conditions. A chitosan-based nasal vaccine against Norwalk virus has demonstrated protective efficacy, highlighting its potential for mucosal immunization [9]. Studies have also shown that chitosan can stimulate immune responses by activating pathways like cGAS-STING, boosting the body's defense mechanisms against pathogens [10].

Recent developments in glycoscience have highlighted the potential of carbohydrate ligands to modulate nano–bio interactions at the biomaterial interface. Carbohydrates such as mannose and galactose can interact with C-type lectin receptors (CLRs), including the mannose receptor (MR) and macrophage galactose-type lectin (MGL), which mediate antigen uptake and immune activation [11]. Although mannose-functionalized nanocarriers have been investigated for immune targeting, considerably less attention has been given to alternative carbohydrate ligands such as lactobionic acid and gluconic acid, particularly in the context of chitosan-based intranasal vaccine delivery systems. Moreover, the extent to which these carbohydrate modifications influence the physicochemical behavior of chitosan nanoparticles (NPs), their interaction with the nasal mucosa, and their immunological performance remains poorly understood.

In this study, previously established chitosan derivatives functionalized with lactobionic acid, mannose, or gluconic acid were used to prepare NPs to investigate how these distinct carbohydrate modifications affect their physicochemical properties and biological interactions relevant to intranasal vaccination. While mannose provides a carbohydrate motif with potential relevance to lectin-mediated cellular interactions, gluconic acid was incorporated primarily to modulate the physicochemical properties of chitosan, whereas lactobionic acid provides a galactose-containing carbohydrate modification. Importantly, the present work does not introduce new carbohydrate-functionalization chemistries, but rather investigates their functional translation into a NP-based protein vaccine platform. By examining NP physicochemical properties together with interactions with nasal epithelial models, *ex vivo* nasal tissue, and human macrophages, followed by evaluation of mucosal and systemic immune responses *in vivo*, this study addresses how established carbohydrate-functionalized chitosan chemistries can influence the performance of antigen-adsorbed NPs across the nasal and immune interfaces. Overall, this work links carbohydrate functionalization with epithelial transport and immune interactions, providing insights relevant to the rational design of polysaccharide-based NP platforms for intranasal vaccine delivery.

2. Materials and methods

2.1. Materials

Chitosan (ChitoClear™, 89% deacetylation degree, 71 cP viscosity, ~164,000 g/mol MW) was obtained from Primex Bio-Chemicals AS (Avaldsnes, Norway) and further purified in our laboratory to remove potential contaminants. The purification process involved treatment with sodium hydroxide, filtration, multiple acidic washes, and freeze-drying. The recombinant SARS-CoV-2 B.1.1.529 (Omicron) S1 + S2 trimer antigen (cat. no. 40589-V08H26) was obtained from Sino Biological (Beijing, China). Highly purified, endotoxin-free water was used in all experiments and was graciously provided by Fresenius-Kabi (Campo de Besteiros, Portugal). RPMI 2650, a human nasal septum carcinoma cell line, was acquired from the American Type Culture Collection (ATCC) (Manassas, VA, USA). Lipopolysaccharides of the O55:B5 serotype originating from *Escherichia coli*, D-gluconic acid solution (49–53 wt% in H_2O; cat. no. G1951), a BrdU ELISA cell proliferation kit, Lactobionic acid (cat. no. 153516), MTT (3-(4,5-Dimethylthiazol-2-yl)-2,5-Diphenyltetrazolium Bromide), D-mannose (cat. no. M6020), and resazurin sodium salt were procured from Sigma-Aldrich Corporation (St. Louis, MO, USA). Magnetic CD14 MicroBeads, MidiMACS™ Separator and SARS-CoV-2 peptides (PepTivator SARS-CoV-2 Prot_S B11529 MUT) were obtained from Miltenyi Biotec (Bergisch Gladbach, Germany). RPMI 1640 medium (cat. no. 42401018), DMEM/F-12 medium (cat. no. 11320033), MEM non-essential amino acids solution, MEM amino acids solution, high-binding 96-well Nunc MaxiSorp™ flat-bottom plates, bovine collagen I solution (5 mg/mL), ProcartaPlex™ Mouse Th1/Th2/Th9/Th17/Th22/Treg Cytokine Panel, 17plex (EPX170-26087-901), TrypLE™ Select Enzyme (phenol red-free), Image-IT™ LIVE Plasma Membrane and Nuclear Labelling Kit, H_2DCFDA (2′,7′-dichlorodihydrofluorescein diacetate), DAF-FM DA (4-Amino-5-Methylamino-2′,7′-Difluorofluorescein Diacetate), HEPES buffer solution, sodium pyruvate solution, and GlutaMAX were purchased from Thermo Fisher Scientific Inc. (Waltham, MA, USA). Lymphoprep was acquired from Stemcell Technologies (distributed by Stemcell Technologies, Saint-Égrève, France). The SARS-CoV-2 Surrogate Virus Neutralization Test kit (sVNT) was purchased from GenScript (Piscataway, NJ, USA). Black 96-well plates and Snapwell™ cell culture inserts (1.13 cm^2 polyester, 0.4 μm pore size) were supplied by Corning Costar (Lowell, MA, USA). The IP-10 and RANTES human ELISA kits, along with recombinant human M-CSF were all sourced from PeproTech (Rocky Hill, NJ, USA). Anti-human CD68 APC (clone Y1/82A, cat. no. 333810), anti-human CD163 PE (clone RM3/1, cat. no. 326506), anti-human CD206 (MMR) FITC (clone 15-2, cat. no. 321104), anti-human CD80 PerCP/Cyanine5.5 (clone 2D10, cat. no. 305232), anti-human CD86 Alexa Fluor 488® (clone IT2.2, cat. no. 305414), anti-human

CD301 (CLEC10A) PE (clone H037G3, cat. no. 354704), anti-human/mouse Granzyme B FITC (clone QA16A02, cat. no. 372206), anti-mouse/human CD44 PE (clone IM7, cat. no. 103008), anti-mouse CD62L PerCP (clone MEL-14, cat. no. 104430), anti-mouse IFN-γ PE (clone XMG1.2, cat. no. 505808), anti-mouse TNF-α PerCP/Cyanine5.5 (clone MP6-XT22, cat. no. 506322), anti-mouse CD8a APC (clone 53-6.7, cat. no. 100712), anti-mouse CD4 FITC (clone RM4-5, cat. no. 100510) monoclonal antibodies, the Cyto-Fast™ Fix/Perm Buffer Set kit and Brefeldin A solution were obtained from Biolegend (San Diego, CA, USA). Murine IgA ELISA kit and IgG HRP, including its isotypes (IgG1, IgG2c, IgG3 and IgE), were provided from SouthernBiotech (Birmingham, AL, USA). All supplementary reagents used in the study were of high analytical purity and procured from standard commercial sources.

2.2. Methods

2.2.1. Synthesis of chitosan and sugar-derivative functionalized nanoparticles

Chitosan and sugar-functionalized NPs were synthesized using a coacervation/precipitation method with sodium tripolyphosphate (TPP) as the cross-linking agent, following an adapted protocol previously developed by our group [12]. To begin, purified chitosan free of LPS was dissolved in 1% (*v*/v) acetic acid under continuous magnetic stirring overnight. The ratio of chitosan to sugar-modifying agents was adjusted based on the desired modification. The pH of the chitosan solution was adjusted to 4.6–4.8 for gluconic acid and lactobionic acid modifications and to 5.5 for mannose modification using 10 M sodium hydroxide. For gluconic acid activation, a solution containing 600 mg of gluconic acid, 242 mg of N–(3-dimethylaminopropy)–N′–ethylcarbodiimide hydrochloride (EDC), and 145 mg of N–hydroxysuccinimide (NHS) was prepared in 15 mL of endotoxin-free water and stirred for 1 h. This activated gluconic acid solution was added dropwise to the chitosan solution (10 mg/mL) under gentle stirring, and the mixture was incubated at room temperature (RT) for 24 h. Similarly, lactobionic acid functionalization involved preparing a solution of 200 mg lactobionic acid, 128.5 mg EDC, and 77 mg NHS dissolved in 20 mL of endotoxin-free water. This solution was stirred for 1 h, added dropwise to the chitosan solution (5 mg/mL), and incubated for 24 h at RT. For mannose functionalization, 135 mg of D-mannose and 32 mg of sodium triacetoxyborohydride were dissolved in 15 mL of endotoxin-free water and stirred for 1 h to activate the mannose. This activated mannose solution was gradually added to 15 mL of the chitosan solution (3 mg/mL) under continuous magnetic agitation and incubated at RT for 48 h. After functionalization, the modified chitosan solutions were dialyzed against endotoxin-free water for 72 h to remove unreacted components, followed by freeze-drying for 48 h to obtain powdered sugar-modified chitosan.

NPs were then prepared using either unmodified chitosan, lactobionic acid-modified chitosan, or a combination of gluconic acid-modified and mannose-modified chitosan in a 3:7 ratio. For all formulations, the polymer solutions were prepared at a concentration of 0.1% (*w*/*v*) in 1% (*v*/v) acetic acid, with the pH adjusted to 4.6–4.8 using 10 N sodium hydroxide. To initiate cross-linking, specific volumes of a 0.16% (*w*/*v*) TPP solution were added to 10 mL of polymer solution while homogenizing at high speed for 1.5 min. The TPP volumes used were 1.75 mL for NPs formed from unmodified chitosan (CHIT NPs), 1.00 mL for lactobionic acid-modified chitosan (CHIT-LA NPs), and 1.60 mL for gluconic acid and mannose-modified chitosan blends (CHIT-MAN NPs). The mixtures were stirred for 1 h to stabilize the particles, which were subsequently concentrated and washed with pyrogen-free water using a Vivaspin 20 centrifugal concentrator (MWCO 300 kDa) at 3000 ×*g*.

For the *in vivo* experiments, the spike protein from the SARS-CoV-2 Omicron variant was adsorbed onto the nanoparticles by incubating 500 μg of NPs with 10 μg of antigen under agitation for 10 min. Antigen adsorption was confirmed using a Micro BCA™ Protein Assay Kit according to the manufacturer's instructions.

2.2.2. Characterization of chitosan-based particles: size, zeta potential, and morphological imaging

The characterization of particle size and zeta potential was performed using dynamic light scattering (DLS) and electrophoretic light scattering (ELS), respectively. All measurements were conducted at 25 °C using the Zetasizer Nano-ZS instrument (Malvern Instruments, Ltd., Worcestershire, UK), following standard procedures. For particle size determination, a backscatter detection angle of 173° was employed, while zeta potential was analyzed to evaluate surface charge. The different particles (CHIT NPs, CHIT-LA NPs and CHIT-MAN NPs) were dispersed in water as well as in supplemented DMEM and RPMI cell culture media for these analyses. The morphological analysis of the particles was carried out using transmission electron microscopy (TEM). TEM imaging was conducted with a JEM 1400 microscope operating at 120 kV (JEOL, Peabody, MA, USA). To prepare the samples for TEM, a small volume of each NP suspension was deposited onto a copper mesh grid and allowed to air dry at RT. Ultra-pure water was used as the suspension medium for the NPs prior to analysis.

2.2.3. Structural analysis and interaction of chitosan-functionalized NPs with simulated nasal mucus

The internal structure of NPs, both with and without the spike SARS-CoV-2 antigen adsorbed onto their surface, as well as their structural modifications upon interaction with a nasal mucus model were investigated using Small Angle X-Ray Scattering (SAXS) technique. Measurements were performed at the ID02 beamline (ESRF, Grenoble, France) (IN-949). Samples were injected in plastic capillaries (diameter = 2 mm) and mounted in a multi-place sample holder to measure the buffer and the samples in the same configuration. The 2D scattered intensity patterns were acquired to obtain, after data reduction, the scattered intensity profiles I as a function of the scattering vector q, defined as $q = 2\pi/\lambda \sin(\theta/2)$, where $\lambda = 0.1$ nm is the wavelength of the incident radiation and θ the scattering angle. The intensity patterns were collected at two different sample-to-detector distances (1 and 10 m) and the intensity profiles I(q) were carefully joined after normalization and background subtraction. The measure of I(q) in a wide q-range ($0.008 < q < 5\ nm^{-1}$) can reveal the structure of the nanoparticles from the overall shape (hundreds of nms) to the internal details (nms). To evaluate structural stability in the presence of simulated nasal mucus, the same formulations were incubated for 15 min with porcine mucin 0.5% (*w*/*v*). Following incubation, the mucus spectrum was subtracted from the SAXS profiles, and the resulting data were compared to the profiles of NPs before incubation.

2.2.4. Ex vivo mucoadhesion study

The mucoadhesive properties of chitosan-based nanoparticles (CHIT NPs, CHIT-LA NPs, and CHIT-MAN NPs) were evaluated using an inclined plane apparatus to simulate the effects of nasal mucus flow under controlled conditions. FITC-labeled chitosan was synthesized following an established protocol that involves a reaction between the isothiocyanate group of FITC and the primary amines present in chitosan, as previously described by our group [13]. Freshly excised rabbit nasal mucosa discs, each 8 mm in diameter, were prepared and used as the substrate for the assay. Rabbit heads from healthy animals, obtained from certified sources (Bertoni Carni S.r.l., Busana, Italy), were stored on ice and processed within 4 h post-mortem. The nasal mucosa, along with its supporting cartilage, was carefully dissected, rinsed with physiological solution, and then punched into circular sections. The tissue samples were kept hydrated on absorbent paper moistened with physiological solution inside closed Petri dishes until the experiment. The inclined plane apparatus consisted of a glass Petri dish positioned at a 45° angle, allowing for the continuous flow of simulated nasal electrolyte solution (SNES) [14] over the mucosal tissue. SNES, formulated to reproduce the ionic composition of nasal secretions, consisted of 8.77 mg/mL sodium chloride, 2.98 mg/mL potassium chloride, and 0.59 mg/mL calcium chloride in water. The pH of the solution was adjusted to 6.5 using 1 M

hydrochloric acid. Each mucosal tissue sample was affixed to the Petri dish using double-sided adhesive tape and treated with 10 μL of FITC-labeled NP suspension (final concentration: 5 μg/mL). After allowing the NPs to adhere for 5 min, the Petri dish was placed on the inclined plane, and SNES was flowed over the mucosal surface at a constant rate of 120 μL/min using a syringe pump (Model 200, KD Scientific, Holliston, MA, USA). The flow was maintained for 30 min, during which samples of the eluted SNES were collected at 5 min intervals. At the conclusion of the experiment, the mucosal discs were homogenized with 0.5 mL of standard diluent to extract residual FITC-labeled NPs that remained adhered to or had penetrated the tissue. The homogenate was then centrifuged at 2000 ×*g* for 10 min at 25 °C, and the supernatant was collected. The collected supernatant samples, along with the previously eluted SNES samples, were plated into black 96-well plates, and fluorescence was measured at excitation and emission wavelengths of 485 ± 20 nm and 510 ± 10 nm, respectively, using a plate reader (Spark 10M, Tecan, Männedorf, Switzerland). Fluorescence readings were normalized by subtracting the blank mucosa control values and expressing the results as the percentage of the total FITC signal recovered for each sample, with the initial fluorescence of each NP batch set as 100%.

2.2.5. Ex vivo tissue permeability assessment using two-photon microscopy

To assess the ability of unmodified chitosan and functionalized chitosan NPs to permeate rabbit nasal mucosa, freshly excised nasal mucosa discs, each 8 mm in diameter, were prepared as described in Section 2.2.4 and used as substrates for the assay. Initially, the three-dimensional (3D) tissue structure was analyzed without any formulation to establish baseline reference data. This included identifying tissue autofluorescence and the presence of collagen, indicative of tissue's structure. After the baseline was established, 2 μL of the FITC-labeled NPs were applied to the mucosal surface. The penetration of the NPs was then evaluated using a two-photon microscope Nikon A1R MP+ multiphoton upright microscope equipped with a Coherent Chameleon Discovery femtosecond pulsed laser (100 fs pulse duration with 80 MHz repetition rate, tunable excitation range 700–1300 nm) equipped with a water-immersion objective Nikon MRH072241 20× with a numerical aperture of 0.75 and 0.5 mm working distance. *Z*-stack images were captured from the surface to a depth of approximately 120 μm within the tissue to detect the presence of NPs. Images were acquired at an excitation wavelength of 900 nm, and laser intensity was maintained at 40% throughout the experiment to ensure consistency. The tissue was scanned at three timepoints (0, 15, and 30 min post-application), and fluorescence spectra were acquired at approximately 120 μm from the tissue surface at the same location at each time point.

2.2.6. Human nasal cell line RPMI 2650

The RPMI 2650 human nasal septum carcinoma cell line (ATCC CCL-30) was maintained in T-75 flasks using complete DMEM/F-12 medium supplemented with 10% (*v*/v) heat-inactivated fetal bovine serum (FBS). The cells were cultured in a humidified incubator set at 37 °C with 95% air and 5% CO_2 to ensure optimal growth conditions. All experiments were performed with cells between passages 15 and 25 to maintain consistency and reproducibility.

2.2.6.1. Cytotoxicity studies on human nasal cells. The cytotoxicity of unmodified chitosan and functionalized chitosan NPs against the RPMI 2650 cells was assessed using the MTT colorimetric assay. Cells were seeded in 96-well culture plates at a density of 8×10^4 cells per well and incubated at 37 °C in a humidified atmosphere of 5% CO_2 for 24 h to allow for proper cell adhesion. Following incubation, serial dilutions of chitosan-based NPs, with final concentrations ranging from 19.5 to 2500 μg/mL, were prepared and added to the wells to assess cytotoxicity. After 20 h of NP exposure, the cells were gently washed with phosphate-buffered saline (PBS) to remove residual particles. Subsequently, 180 μL of fresh medium and 20 μL of MTT reagent (5 mg/mL in PBS) were added to each well. Plates were then incubated for an additional 2 h at 37 °C to allow viable cells to reduce the MTT reagent into formazan crystals. Subsequently, the MTT-containing medium was carefully removed, and 120 μL of dimethyl sulfoxide (DMSO) was added to each well to dissolve the violet-colored formazan. The optical density (OD) of the solution in each well was measured at 540 nm and 630 nm using a microplate reader (Spark 10 M, Tecan, Männedorf, Switzerland). The percentage of cell viability was calculated by comparing the absorbance values of treated samples to those of untreated control cells, which were cultivated in complete DMEM/F-12 without NPs, following Eq. (1).

$$Cell\ Viability\ (\%) = \left(\frac{ODsample(540nm) - ODsample(630nm)}{ODcontrol(540nm) - ODcontrol(630nm)}\right) \times 100 \quad (1)$$

2.2.6.2. Permeability and barrier function analysis of fluorescent-labeled NPs with TEER. To simulate an *in vitro* nasal epithelium, RPMI 2650 cells were cultivated under Air-Liquid Interface (ALI) conditions, which allow the cells to differentiate into a pseudo-stratified layer and secrete mucus on their apical surface [15]. Six-well Snapwell™ inserts were used to establish the ALI model. To enhance cell adhesion, the membranes were coated with 50 μL of bovine collagen I solution (5 mg/mL) diluted in ethanol (final concentration 1 mg/mL) and left overnight in an incubator at 37 °C. Before seeding the cells, the membranes were rinsed with pre-warmed culture medium. A suspension of RPMI 2650 cells (1.5×10^6 cells per well) in 400 μL of complete culture medium was added to the collagen-coated inserts. After 48 h of incubation, the medium in the apical compartment was removed to initiate ALI conditions, while the medium in the basolateral chamber was replaced three times per week. The cells were cultured under ALI for up to 21 days, allowing for differentiation. Transepithelial electrical resistance (TEER) values were monitored every 2–3 days using an EndOhm epithelial voltohmmeter (World Precision Instruments, Sarasota, FL, USA). TEER values were measured by adding pre-warmed medium to the apical compartment and equilibrating for at least 30 min at 37 °C in a humidified incubator with 5% CO_2. Blank filter resistance values were subtracted, and TEER values were normalized to the insert area (1.13 cm^2). Wells with TEER values above 70 $\Omega \cdot cm^2$ were deemed suitable for the permeation study. In parallel, the epithelial cell layer was monitored by optical microscopy to assess cell morphology and confluence before the permeability experiments. The integrity and functionality of the epithelial barrier were validated using FITC (MW 389.382 g/mol) as a paracellular marker. For the assay, 250 μL of a 10 μg/mL FITC solution or FITC-labeled chitosan-based NPs were added to the apical (donor) compartment, while 2.5 mL of pre-warmed DMEM/F-12 medium was added to the basolateral (acceptor) chamber. The plates were incubated at 37 °C in a humidified atmosphere with 5% CO_2. Samples of 500 μL were collected from the basolateral compartment at defined timepoints (0, 1, 3, 6, and 20 h). An equal volume of fresh, pre-warmed medium was added to replace the sampled volume to maintain sink conditions. After 20 h, the apical formulations were collected for further analysis and the apical compartments were subsequently washed with PBS, and the cells were lysed with 100 μL of sterile Milli-Q water to evaluate the intracellular content of the FITC or FITC-labeled NPs. All samples were transferred to black 96-well plates, and fluorescence was measured using a Spark 10 M microplate reader (Tecan, Männedorf, Switzerland) at excitation and emission wavelengths of 485 ± 20 nm and 510 ± 10 nm, respectively. The permeability coefficient (Papp) was calculated using Eq. (2):

$$Papp = \left(\frac{dQ}{dt \cdot C0 \cdot A}\right) \quad (2)$$

where dQ/dt is the flux (μg/s) of FITC across the epithelial barrier, C0 is the initial donor concentration (μg/mL), and *A* is the surface area of the

insert (cm^2). At the conclusion of the assay, TEER values were measured again to verify the integrity of the epithelial monolayer.

2.2.7. Separation of human PBMCs and monocyte purification

Peripheral blood (buffy coat) was obtained from the IPST, IP (Coimbra, Portugal) with informed consent from healthy donors, in accordance with institutional ethical guidelines and the Declaration of Helsinki. Approval for the study was granted by the Ethics Committee of the Faculty of Medicine, University of Coimbra (approval number CE-063/2019). Peripheral blood mononuclear cells (PBMCs) were isolated using a density gradient centrifugation method with Lymphoprep, following a slightly modified version of the manufacturer's instructions. Blood samples were diluted with 0.9% sodium chloride at a 2:1 (*v*/v) ratio, and 25 mL of this diluted blood was carefully layered onto 10 mL of Lymphoprep in 50 mL tubes. The samples were centrifuged at 1190 ×*g* for 20 min at 20 °C without braking to ensure the clean separation of the mononuclear cell layer. This layer was carefully collected and subjected to two washing steps in PBS (pH 7.4, pre-warmed to 37 °C) by centrifugation at 350 ×*g* for 10 min at 20 °C. The resulting cells were resuspended in RPMI 1640 medium supplemented with 10% heat-inactivated FBS, 100 μg/mL streptomycin, 100 U/mL penicillin, and GlutaMAX 1×. Cell viability was determined *via* the trypan blue exclusion assay using a Neubauer chamber, and only samples exceeding 90% viability were used for subsequent experiments. Monocytes were enriched from PBMCs using the MidiMACS™ Separator equipped with magnetic CD14 MicroBeads, as per the manufacturer's protocol.

2.2.8. In vitro generation of macrophages from human monocytes

Isolated monocytes were seeded into 12-well plates at a density of 0.75×10^6 cells/mL in 1.5 mL of macrophage culture medium. This medium consisted of RPMI 1640 supplemented with 100 μg/mL streptomycin, 100 U/mL penicillin, 10% heat-inactivated FBS, GlutaMAX 1×, and 25 mM HEPES buffer. To facilitate differentiation into macrophages, macrophage colony-stimulating factor (M-CSF) was added at a final concentration of 50 ng/mL. Cells were incubated for a total of 6 days, with half of the medium replaced on day 3 and supplemented with fresh M-CSF (50 ng/mL) to maintain differentiation conditions. On day 6, the differentiated macrophages were harvested. First, the culture medium was carefully discarded, and the wells were rinsed with PBS to remove residual serum. Subsequently, 300 μL of pre-warmed TrypLE™ Select Enzyme was added to each well and incubated at 37 °C for 15 min to detach the adherent macrophages. The detached cells were collected, centrifuged at 350 ×*g* for 5 min at RT, and resuspended in unsupplemented culture medium. Cell viability was evaluated using trypan blue staining, ensuring over 90% viability before further use. Flow cytometry was performed to confirm the macrophage phenotype, using CD206 (MMR) FITC and CD68 APC staining prior to experimental procedures.

2.2.8.1. Investigation of cellular internalization of chitosan-functionalized NPs using flow cytometry and confocal microscopy. To investigate the internalization of glyco-modified chitosan nanoparticles (CHIT NPs, CHIT-LA NPs, and CHIT-MAN NPs) in macrophages, two complementary techniques—flow cytometry and confocal microscopy—were employed. Cellular internalization studies utilized FITC-labeled particles, as previously described in Section 2.2.4.

For flow cytometry, macrophages were seeded in 24-well plates at a density of 3.5×10^5 cells per well and incubated overnight to allow cell adherence. The following day, the culture medium was replaced with fresh medium containing FITC-labeled glyco-modified chitosan NPs at a final concentration of 5 μg/mL. FITC alone, at the same concentration, was included as a control. The cells were incubated for 4 h at 37 °C. After incubation, the culture medium was aspirated, and the wells were rinsed with pre-warmed (37 °C) PBS to remove unbound NPs. The macrophages were then detached using 150 μL of pre-warmed TrypLE™ Select Enzyme for 15 min. The detached cells were collected, centrifuged at 350 ×*g* for 5 min at RT, and resuspended in PBS containing 1% FBS. The cells were subsequently fixed with 2% paraformaldehyde for 20 min at RT. Flow cytometric analysis was performed using a BD Accuri C6 instrument (BD Bioscience, Franklin Lakes, NJ, USA), with results expressed as the mean fluorescence intensity of FITC-positive cells from a sample of 10,000 cells. For the blocking assay, prior to adding the FITC-labeled glyco-modified NPs, macrophages were pre-incubated with purified antibodies specifically targeting MGL and MR. These antibodies were applied according to the manufacturer's instructions, and the cells were incubated for 1 h at 37 °C to ensure receptor blocking. After this pre-incubation step, FITC-labeled NPs were added at the same concentration of 5 μg/mL, and the cells were further incubated for 4 h. Following this, the protocol for flow cytometric analysis described above was carried out to assess NP internalization.

For confocal microscopy, macrophages were seeded onto sterile glass coverslips placed in 24-well plates at the same density of 3.5×10^5 cells per well and incubated overnight. The next day, the medium was replaced with fresh culture medium containing FITC-labeled glyco-modified chitosan NPs at a final concentration of 5 μg/mL. The cells were incubated for 4 h under the same conditions. After incubation, the supernatants were carefully removed, and the cells were washed three times with pre-warmed PBS. The cells were fixed with 4% paraformaldehyde for 20 min at RT and washed three times with PBS. Following fixation, the cells were stained using the Image-IT™ LIVE Plasma Membrane and Nuclear Labelling Kit, according to the manufacturer's instructions. Briefly, the nuclei were stained with Hoechst 33342, and the plasma membranes were labeled with Alexa Fluor® 594-conjugated wheat germ agglutinin for 10 min. After staining, the coverslips were washed twice with PBS and mounted onto glass slides using DAKO mounting medium. Once the mounting medium had dried, the coverslips were sealed and stored at −20 °C until imaging. Cellular internalization of NPs was visualized using a Carl Zeiss LSM 710 confocal microscope (Carl Zeiss, Oberkochen, Germany).

2.2.8.2. Reactive oxygen species (ROS) production assay. Macrophages were seeded in black 96-well plates at a density of 8×10^4 cells per well and incubated overnight to promote adherence. After this initial incubation, the culture medium was replaced with 25 μM H_2DCFDA dissolved in serum-free RPMI, and the cells were further incubated for 1 h to allow uptake of the probe. Following the incubation, the medium was carefully aspirated, and glyco-modified chitosan nanoparticles (CHIT NPs, CHIT-LA NPs, and CHIT-MAN NPs) were introduced into the wells at a final concentration of 5 μg/mL. Lipopolysaccharide (LPS) at 1 μg/mL was included as a positive control. The plate was then incubated for an additional 2 h. Fluorescence measurements were performed using excitation and emission wavelengths of 485 ± 20 nm and 528 ± 20 nm, respectively, to assess the production of ROS. The fluorescence intensity of treated samples was compared to that of the negative control to calculate the fold increase in ROS production. After measuring fluorescence, the supernatant was removed, and each well was treated with 200 μL of fresh culture medium supplemented with 12 μg/mL of resazurin sodium salt. The plate was incubated for 24 h at 37 °C in a 5% CO_2 environment to evaluate cell metabolic activity. Optical density was then measured at 570 nm, with a reference reading at 620 nm, using a transparent cell culture plate. ROS production and cell viability were calculated using the respective Eqs. (3) and (4).

$$ROS\ Production\ (Fold\ increase\ in\ fluorescence) = \left(\frac{Fluorescence\ sample}{Fluorescence\ untreated\ cells}\right) \quad (3)$$

$$Cell\ Viability\ (\%) = \left(\frac{ODsample(570nm) - ODsample(620nm)}{ODcontrol(570nm) - ODcontrol(620nm)}\right) \times 100 \quad (4)$$

2.2.8.3. Nitric oxide (NO) production assay. Monocyte-derived macrophages were seeded into black 96-well plates at a density of 8×10^4 cells per well and incubated overnight under standard conditions to allow cell adherence. The next day, the culture medium was replaced with 5 μM DAF-FM DA prepared in serum-free RPMI, and the cells were incubated for 1 h to enable probe uptake. Afterward, the medium was carefully removed, and glyco-modified chitosan nanoparticles (CHIT NPs, CHIT-LA NPs and CHIT-MAN NPs) were added to the wells at a final concentration of 5 μg/mL. LPS was included as a positive control at a concentration of 1 μg/mL. The cells were then incubated for 24 h to allow NO production. Fluorescence was measured using excitation and emission wavelengths of 495 ± 20 nm and 515 ± 20 nm, respectively. After fluorescence readings, cell viability was assessed following the method outlined in the preceding section to evaluate potential cytotoxic effects of the treatments. The increase in NO production induced by the particles was determined by normalizing the fluorescence intensity values to those of untreated control cells, as described using Eq. (5).

$$NO\ Production\ (Fold\ increase\ in\ fluorescence) = \left(\frac{Fluorescence\ sample}{Fluorescence\ untreated\ cells}\right) \quad (5)$$

2.2.8.4. Assessment of phenotypic traits and chemokine secretion in differentiated macrophages. Macrophages were cultured in 24-well plates at a density of 3.5×10^5 cells per well and incubated overnight to allow adherence. The following day, glyco-modified chitosan nanoparticles (CHIT NPs, CHIT-LA NPs, and CHIT-MAN NPs) were added to the wells at a final concentration of 5 μg/mL. LPS at 1 μg/mL was included as a positive control, and untreated cells served as negative controls. The cells were incubated for 24 h to assess phenotypic changes and chemokine secretion. At the end of the incubation period, the supernatants were carefully collected for analysis of chemokine production. IP-10 and RANTES levels in the supernatants were quantified using ELISA following the manufacturer's instructions. To analyze the phenotype of the macrophages, cells were detached from the wells by rinsing with PBS and adding 150 μL of pre-warmed TrypLE™ Select Enzyme to each well. The plate was incubated at 37 °C for 15 min to facilitate cell detachment. Detached cells were collected and centrifuged at 350 ×*g* for 5 min at 20 °C. After centrifugation, cells were washed and resuspended in PBS containing 1% FBS. Cells were then incubated with Human TruStain FcX™ (Fc receptor blocking reagent) according to the manufacturer's instructions, using a volume adjusted to the cell number, to minimize nonspecific binding. For phenotypic analysis, macrophages were stained with specific antibody panels for 30 min at 4 °C: CD68 APC/CD206 FITC and CD163 PE/CD86 Alexa Fluor 488®/CD80 PerCP/Cyanine5.5, according to the manufacturer's recommendations. Following the staining procedure, cells were washed again and resuspended in PBS with 1% FBS. Phenotypic characteristics were analyzed using a BD Accuri™ C6 flow cytometer. The results were expressed as the increase in mean fluorescence intensity (MFI) of treated macrophages relative to untreated control cells, calculated using Eq. (6).

$$MFI\ increase = \left(\frac{MFI\ sample}{MFI\ untreated\ cells}\right) \quad (6)$$

2.2.9. Vaccination study

Five-week-old female C57BL/6 mice were obtained from Charles River Laboratories (Barcelona, Spain) and acclimated for one week upon arrival in the local animal housing facility. The mice were maintained under standard conditions, including a 12 h light/dark cycle, with unrestricted access to food and water. All experimental procedures were conducted in compliance with institutional ethical guidelines and were approved by the relevant ethics committee (approval number DGAV 0421/000/000/2020). The study also adhered to national legislation (Dec. No. 113/2013) and European Union Directive 2010/63/EU regarding the protection of animals used for scientific purposes. Vaccines were prepared in pyrogen-free water and administered intranasally in a dose volume of 10 μL per administration (5 μL per nostril), following a schedule of three doses delivered two weeks apart. The vaccination formulations and protocol are summarized in Fig. 1. Unvaccinated mice, along with mice administered solely with the antigen, served as control groups. On day 42 of the study, all groups were anesthetized using isoflurane prior to euthanasia by cervical dislocation.

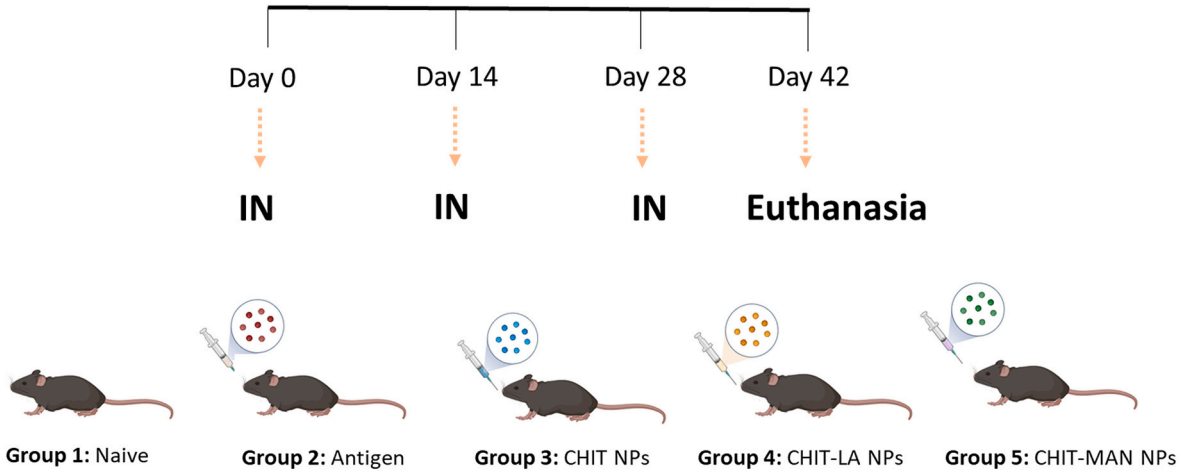
2.2.9.1. Blood sampling. On day 42, blood samples were collected from the submandibular vein using an animal lancet and transferred into microcentrifuge tubes. Isoflurane anesthesia was administered during the procedure to minimize animal distress. The samples were allowed to coagulate at RT for 5–6 h before being centrifuged at 4500 ×*g* for 10 min at 4 °C to separate the serum. The resulting supernatant was carefully pipetted into fresh microcentrifuge tubes and stored at −20 °C for subsequent analysis.

2.2.9.1.1. Quantification of immunoglobulin levels in serum. Spike-specific serum IgG, IgG subclasses, and IgE were quantified by indirect ELISA following our previously described protocol [16]. Briefly, plates were coated with recombinant SARS-CoV-2 spike protein (1 μg/mL), incubated with serial serum dilutions, and detected using HRP-conjugated secondary antibodies. Serum immunoglobulin titers were determined by calculating the endpoint titer, defined as the last log2 dilution at which the OD was at least two-fold greater than that of naive serum at the same dilution. To standardize results and minimize variability, the data were reported as log2 endpoint titers.

2.2.9.1.2. SARS-CoV-2 neutralization surrogate assay. Neutralizing antibodies in serum were detected using a SARS-CoV-2 Surrogate Virus Neutralization Test kit, according to the manufacturer's instructions. This assay quantifies the presence of antibodies capable of blocking the interaction between the RBD of the viral spike glycoprotein and the ACE2 receptor [17]. To begin, mouse serum samples were diluted tenfold and mixed with an equal volume of diluted HRP-conjugated RBD from the Omicron (B.1.1.529) variant. The mixture was incubated at 37 °C for 30 min to allow antibody binding. After incubation, the solution was transferred to a capture plate pre-coated with human ACE2 protein and incubated at 37 °C for an additional 15 min. Following the incubation, the plate was washed four times to remove unbound components. Then, 100 μL of TMB substrate solution was added to each well and incubated in the dark at RT for 15 min. The enzymatic reaction was halted by adding 50 μL of stop solution, and the absorbance was measured at 450 nm using a microplate reader to determine the presence of neutralizing antibodies.

2.2.9.2. Mucosal secretion sampling. On day 42, vaginal and nasal washes were collected for analysis. Vaginal washes were obtained by flushing the vaginal cavity four times with 25 μL of sterile cold PBS. For nasal washes, the mouse was held upright, and 10 μL of sterile cold PBS was gently pipetted into one nostril five times, allowing the fluid to flow out from the opposite nostril. The procedure was repeated for the other nostril. The resulting 100 μL wash sample from each procedure was then treated with 1 μL of 1% sodium azide, 1 μL of 100 mM phenylmethylsulfonyl fluoride (PMSF), and 6.5 μL of 1% bovine serum albumin (BSA). After incubation at RT for 15 min, the samples were centrifuged at 5000 ×*g* for 15 min. The supernatants were carefully collected and stored at −80 °C for future analysis.

2.2.9.2.1. Quantification of sIgA levels in mucosal secretions. SARS-CoV-2 spike-specific and total IgA levels in nasal and vaginal wash samples were quantified by ELISA following our previously described protocol [18], using a mouse IgA ELISA kit according to the manufacturer's instructions. Briefly, plates were coated with either recombinant SARS-CoV-2 spike protein (for antigen-specific IgA) or the capture antibody provided in the kit (for total IgA). After blocking, samples or IgA standards were incubated, followed by HRP-conjugated detection antibody and colorimetric development with OPD substrate. Absorbance



Groups	Sample Size	Adjuvant NP (μg/dose)	SARS-CoV-2 Spike Protein (μg/dose)
Naive	5	-	-
Antigen	5	-	10
CHIT NPs	5	500	10
CHIT-LA NPs	5	500	10
CHIT-MAN NPs	5	500	10

Fig. 1. Intranasal vaccination schedule and experimental groups. Mice were intranasally immunized on days 0, 14, and 28 with either unmodified chitosan NPs or glyco-modified chitosan NPs, both adsorbed with the spike protein of the SARS-CoV-2 Omicron variant as the antigen, representing protein-subunit vaccines. Two control groups were included: unvaccinated mice (naive) and mice administered with the antigen alone without any adjuvant. On day 42, the animals were sacrificed, and samples were collected for subsequent analysis.

was measured at 492 nm, and IgA concentrations were determined from calibration curves. Results were expressed as the ratio of SARS-CoV-2 spike-specific IgA to total IgA for each sample.

2.2.9.3. Isolation of splenic cells. At the conclusion of the study, animals were anesthetized with inhaled isoflurane and euthanized by cervical dislocation. Spleens were harvested and processed to generate a single-cell suspension by gently pressing the spleen through a 70 μm cell strainer into 10 mL of RPMI 1640 culture medium. The cell suspension was then centrifuged at 220 ×*g* for 10 min at 4 °C to pellet the cells. To remove red blood cells, the pellet was resuspended in 0.5 mL of Ammonium-Chloride-Potassium (ACK) lysis buffer for 1 min, followed by the addition of 10 mL of RPMI 1640 medium to dilute the lysis buffer. After centrifugation to remove any remaining ACK buffer, the cells were washed once more with RPMI. Finally, the splenic cells were resuspended in complete cell culture medium (RPMI 1640, 10% heat-inactivated FBS, 50 μM 2-mercaptoethanol, 100 μg/mL streptomycin, 100 units/mL penicillin, 2 mM L-glutamine, 1% sodium pyruvate, 1% MEM non-essential amino acids, and 2% MEM amino acids at a final concentration of 1×10^7 cells/mL.

2.2.9.4. Isolation of pulmonary lymphocytes. On the final day of the experiment, mice were euthanized, and their lungs were perfused with 4 mL of sterile PBS *via* cardiac injection to remove residual blood. The lungs were excised, placed in a 6-well plate, and rinsed with 5 mL of PBS at 37 °C. Subsequently, the lungs were transferred to PBS containing Ethylene glycol-bis(β-aminoethyl ether)-N,N,N,N-tetra acetic acid tetrasodium salt (EGTA) (19 mg of EGTA per 100 mL PBS), cut into large fragments, and incubated on an orbital shaker at 37 °C for 10 min at 120 rpm. Following three washes with PBS to eliminate remaining blood and EGTA, the lung fragments were incubated in 4 mL of digestion medium (RPMI 1640 supplemented with 10% heat-inactivated FBS, 20 mM HEPES, 100 μg/mL streptomycin, 100 units/mL penicillin, 50 μM 2-mercaptoethanol, 2 mM L-glutamine, 1% sodium pyruvate, 1% MEM non-essential amino acids, and 2% MEM amino acids) containing 0.5 mL of collagenase IV (final concentration 0.5 mg/mL) and 0.5 mL of DNase I (final concentration 0.1 mg/mL). The digestion mixture was incubated at 37 °C for 1 h and 15 min, with gentle mixing performed after 30 min using a Pasteur pipette. The digested suspension was filtered through a 70-μm cell strainer, with any remaining tissue fragments pushed through the strainer and washed with RPMI medium to achieve a total volume of 7.5 mL. The cell suspension was carefully layered onto 2.5 mL of Lymphoprep in a 15 mL tube and centrifuged at 800 ×*g* for 25 min at 20 °C, with no brake applied. The mononuclear cell layer was harvested, resuspended in PBS (pH 7.4) at 4 °C, and centrifuged at 300 ×*g* for 10 min. The resulting cell pellet was resuspended in complete RPMI medium (identical to the digestion medium but without collagenase IV and DNase I) at a final concentration of 1×10^7 cells/mL for subsequent analysis.

2.2.9.5. T cell subset analysis using flow cytometry. Following the isolation of lymphocytes from the spleen and lungs, 100 μL of cell suspension (1×10^7 cells/mL) and 70 μL of cell culture medium were seeded into U-bottom 96-well plates. The plates were incubated overnight at 37 °C in a humidified 5% CO_2 environment. On the following day, 10 μL of purified anti-mouse CD28 antibody (final concentration: 0.2 μg/mL) and 20 μL of SARS-CoV-2 peptides (PepTivator SARS-CoV-2 Prot_S B11529 MUT) were added to each well. The peptide concentration was prepared

according to the manufacturer's recommendations. After a 1 h incubation period, 10 μL of a 21× Brefeldin A solution was added to inhibit protein secretion, and the cells were incubated for an additional 5 h at 37 °C. Following incubation, the cells were harvested for flow cytometry analysis. The cells were pelleted by centrifugation at 350 ×*g* for 5 min and resuspended in PBS containing 1% FBS. For surface marker staining, the cells were incubated at 4 °C for 30 min with specific antibody combinations: Mix 1 (CD4 FITC/CD8a APC), Mix 2 (CD8a APC) and Mix 3 (CD4 FITC/CD8a APC/CD44 PE/CD62L PerCP). After extracellular staining, the cells were washed, fixed, and permeabilized using the Cyto-Fast™ Fix/Perm Buffer Set, following the manufacturer's protocol. Intracellular staining was subsequently performed using the following antibody panels: IFN-γ PE/TNF-α PerCP/Cyanine5.5 for Mix 1 and Granzyme B FITC for Mix 2. Once intracellular staining was completed, the cells were washed, resuspended in PBS containing 1% FBS and 0.05% sodium azide, and analyzed using a BD Accuri™ C6 flow cytometer.

2.2.9.6. Proliferative response and cytokine profiling after SARS-CoV-2 Restimulation. Following the isolation of spleen cells and pulmonary lymphocytes, 50 μL of the cell suspension (1×10^7 cells/mL) was seeded into 96-well plates. The cells were then exposed to either untreated medium or medium supplemented with SARS-CoV-2 peptides, bringing the total volume in each well to 150 μL. The plates were incubated at 37 °C for 96 h to stimulate cytokine production by antigen-specific T cells. After incubation, supernatants were collected and stored at −80 °C for subsequent analysis. Cytokine levels in the supernatants were quantified using the ProcartaPlex™ Mouse Th1/Th2/Th9/Th17/Th22/Treg Cytokine Panel, following the manufacturer's instructions. The remaining cells were analyzed for proliferation using the BrdU Cell Proliferation ELISA kit, performed according to the manufacturer's protocol.

2.2.10. Statistical analysis

The data are presented as the mean ± standard error of the mean (SEM) from at least three independent experiments. Statistical significance was determined using the methods specified in the figure captions, where the symbols *, **, ***, and **** indicate *p*-values of <0.05, <0.01, <0.001, and <0.0001, respectively. Data analysis was carried out using GraphPad Prism 8 software (GraphPad Software, Inc., La Jolla, CA, USA).

3. Results/Discussion

The nasal mucosa represents the primary biological barrier for intranasal vaccine delivery, where mucus, epithelial tight junctions, and mucociliary clearance collectively limit antigen residence time and transport. These factors make efficient interaction with the mucosal interface a critical requirement for successful vaccination strategies.

The carbohydrate-functionalized chitosan derivatives investigated in the present study were previously developed and characterized by our group in the context of nucleic acid delivery systems [16,19,20]. These previous studies established the rationale for introducing distinct carbohydrate functionalities into the chitosan backbone. Lactobionic acid and mannose were selected to provide carbohydrate recognition motifs with the potential to promote interactions with lectin receptors expressed by antigen-presenting cells, whereas gluconic acid was introduced as a hydroxyl-rich modification to modulate the hydrophilicity and physicochemical behavior of the polymer under physiological conditions. Importantly, the combination of gluconic acid and mannose was not arbitrarily selected for the present study. Systematic evaluation of dual-functionalized chitosan/DNA systems identified the 3:7 gluconic acid:mannose composition, corresponding to CGA-MAN 0.3–0.7, as a promising formulation based on its physicochemical and biological performance. In particular, this composition was associated with enhanced immunomodulatory activity, including increased NO and TNF-α production in murine macrophages and increased expression of maturation-associated markers and secretion of IL-12 and TNF-α by human dendritic cells [20]. The present work extends these previous DNA polyplex studies by evaluating these established carbohydrate-functionalized chitosan chemistries in a NP-based protein vaccine platform and investigating whether their functional properties are retained and manifested at the nasal and immune-cell interfaces.

3.1. Physicochemical properties of carbohydrate-modified chitosan delivery systems and their behavior in simulated nasal environment

While the exact mechanisms underlying the nasal delivery of surface-adsorbed NP vaccines remain under investigation, it is widely recognized that the properties of the nanocarrier material play a pivotal role in their effectiveness.

Previously developed and characterized carbohydrate-functionalized chitosan derivatives were used as predefined polymeric materials for NP preparation. Their chemical modification had been confirmed by ATR-FTIR and NMR, with ninhydrin analysis used to quantify the remaining amino groups and assess the extent of functionalization. The main characteristics of these polymers, including their degree of deacetylation and amino group content, are summarized in Table S1. Briefly, lactobionic acid and gluconic acid were conjugated to chitosan amino groups using EDC/NHS chemistry, whereas mannose functionalization was achieved by reductive amination using sodium triacetoxyborohydride [19,20]. NPs were subsequently prepared from these chitosan derivatives by ionic gelation with TPP as the crosslinker, a mild and straightforward method that avoids the use of organic solvents or surfactants. The NPs made from chitosan functionalized with lactobionic acid were referred to as CHIT-LA NPs, while those made from chitosan functionalized with a combination of gluconic acid and mannose were called CHIT-MAN NPs (chemical structures shown in Fig. S1). Unmodified chitosan NPs (CHIT NPs) were also prepared to serve as a control for comparison.

The physicochemical properties of the NPs, including mean particle size, polydispersity index (PDI), and zeta potential, were assessed in both their preparation medium (pyrogen-free water) and in cell culture media (RPMI and DMEM supplemented with FBS) (Fig. 2A). In pyrogen-free water, functionalization with lactobionic acid and mannose reduced the mean particle size from 424 nm for CHIT NPs to 223 nm for CHIT-LA NPs and 315 nm for CHIT-MAN NPs. All three formulations exhibited positive surface charges, with CHIT NPs showing the highest zeta potential (+55 mV), followed by CHIT-MAN NPs (+52 mV) and CHIT-LA NPs (+48 mV). Importantly, the zeta potential values reflect the surface charge of the final TPP-crosslinked NPs rather than the degree of carbohydrate functionalization of the chitosan derivatives. The similar positive charges result from the combined effects of the remaining protonated amino groups, carbohydrate functionalization, and polymer–TPP interactions, with TPP amounts optimized for each formulation to obtain stable NPs. The PDIs for the functionalized NPs were slightly lower than that of the unmodified CHIT NPs, suggesting reduced aggregation and greater uniformity. The observed reduction in particle size for CHIT-LA and CHIT-MAN NPs compared to unmodified CHIT NPs can be attributed to the structural and physicochemical effects of carbohydrate functionalization. The introduction of lactobionic acid, gluconic acid and mannose modifies the charge distribution, hydration properties, and conformational behavior of the chitosan chains, which can influence their organization during NP formation. In particular, the increased hydrophilicity introduced by the carbohydrate moieties may promote stronger polymer–water interactions and influence chain conformation, potentially favoring a more compact organization of the polymer chains within the crosslinked network. These effects may contribute to the smaller particle sizes observed for the functionalized NPs.

Given the complexity of cell culture media and the variability

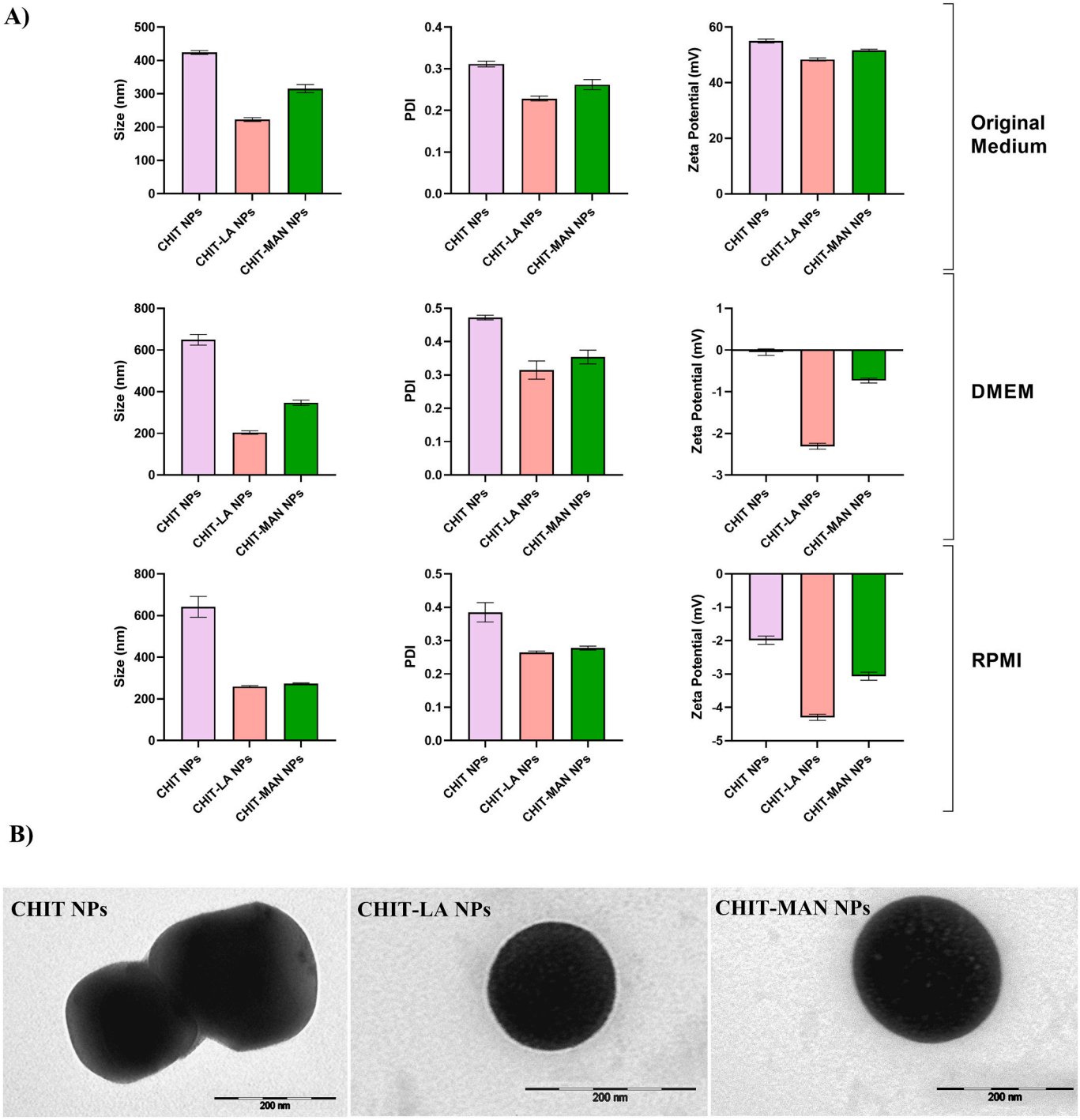


Fig. 2. Physicochemical characterization and structural analysis of chitosan-based particles. The particle size, polydispersity index (PDI), and zeta potential of both carbohydrate-functionalized and unmodified chitosan formulations were assessed in pyrogen-free water—the original medium of the nanoparticles—as well as after resuspension in DMEM and RPMI cell culture media (A). Data are reported as mean ± standard error of the mean (SEM), based on a minimum of four independent experiments ($n \geq 4$). (B) Representative TEM images illustrate the morphology of the chitosan-based nanoparticles in sterile water, with a scale bar corresponding to 200 nm.

introduced by different supplementation components, results from the colloidal characterization of NPs in water cannot be directly extrapolated to *in vitro* conditions [21].Therefore, CHIT, CHIT-LA, and CHIT-MAN NPs were dispersed in DMEM and RPMI, both supplemented with FBS, at a concentration of 156 μg/mL and incubated at 37 °C to characterize their behavior under the cell-culture conditions used in the subsequent *in vitro* studies. The size, PDI, and zeta potential of the NPs were then measured. CHIT NPs exhibited a marked increase in particle size and PDI, with sizes reaching 642 nm in RPMI and 650 nm in DMEM, indicating increased aggregation and size heterogeneity in these media. In contrast, CHIT-LA and CHIT-MAN NPs maintained more consistent sizes and PDIs, likely due to the presence of carbohydrate functional groups, which may reduce protein interactions and shield the NP surface, preventing significant aggregation. All NPs exhibited a decrease in zeta potential in culture media, ranging from 0 to −4.5 mV, due to protein adsorption neutralizing the positive charge of chitosan residues.

However, the functionalization of CHIT-LA and CHIT-MAN NPs with carbohydrate groups appears to have enhanced their hydrophilicity, leading to the formation of a hydration layer around the NP surface. Unlike unmodified CHIT NPs, which are more prone to strong and irreversible protein binding, this hydration layer may have mitigated protein interactions by forming a physical and thermodynamic barrier. Similar to zwitterionic materials, where electrostatic interactions and hydrogen bonding create robust hydration layers that resist protein adsorption, the carbohydrate modifications in CHIT-LA and CHIT-MAN NPs likely contributed to weaker and more reversible protein binding [22]. These differences in NP behavior under the respective cell-culture conditions provide relevant context for interpreting the subsequent cellular uptake and biological responses observed in the *in vitro* studies.

To further confirm the size, shape, and structural characteristics of the unmodified and functionalized chitosan nanocarriers, transmission electron microscopy (TEM) analysis was conducted. TEM revealed that all NP formulations maintained a predominantly spherical morphology, a characteristic trait commonly associated with chitosan-based delivery systems [23,24] (Fig. 2B). The observed particle dimensions ranged from 200 to 400 nm, closely aligning with the measurements obtained through DLS and corroborating prior findings from analogous platforms [12]. This consistency across methodologies underscores the robust and reproducible physicochemical properties of the chitosan-based NPs.

3.2. Structure of carbohydrate-modified chitosan delivery systems and their behavior in simulated nasal environment

The structure of unmodified and functionalized chitosan-based NPs was investigated by SAXS technique, ideal for describing the internal arrangement on the nm length scale. All formulations were measured at 1% concentration in the original medium and the scattered intensity profiles are reported in Fig. 3 (left panel), vertically shifted for better visibility. Data show common features, indicating a similar internal arrangement of NPs. Chitosan chains submitted to the cross-linking process, formed a polymer network with characteristic distances between the junction points of the order of 20 nm. In the low-q region, corresponding to the overall organization of NPs, the scattered intensity profiles follow an $I(q) \div q^{-3}$ decay. This exponential value is related to the fractal arrangement of the polymer network, a quite compact mass fractal for the three systems. Differences between the NPs are visible in the high-q region, corresponding to the local arrangement of the polymer chains. In CHIT NPs and CHIT-MAN NPs, the scattered intensity decay is $I(q) \div q^{-2}$ at $q > 1.3\ nm^{-1}$, demonstrating that the polysaccharide chains on the local scale (up to 5 nm) behaved as a polymer in theta solvent, with a random walk arrangement. Instead in CHIT-LA NPs $I(q) \div q^{-1}$ at $q > 1.24\ nm^{-1}$. In the presence of lactobionic acid modification, the chitosan chains on the local length scale behaved as quite rigid cylinders, up to a distance of 5 nm.

The addition of the Omicron spike protein antigen did not dramatically affect the internal structure of chitosan-based NPs, with data showing similar intensity profiles at $q > 0.1\ nm^{-1}$ (Fig. 3, central panel). Notably, differences are visible in the low-q region, dominated by the general features of the coacervates. In CHIT-LA NPs the low-q decay shows a gentler slope in the presence of the protein, suggesting a slightly looser arrangement of the mass fractal, while in CHIT-MAN NPs the low-q decay is steeper, $I(q) \div q^{-3.9}$ suggesting a more compact surface fractal arrangement, with low surface roughness.

To investigate the structural properties of NPs when in a simulated nasal environment, formulations were incubated for 15 min with porcine mucin 0.5% (*w/v*). Following incubation, the scattered intensity profiles were measured and compared with those of mucin and NPs, as well as with the simple sum of the intensity contributions of the two components, representing the expected profile in the case of ideal mixing of non-interacting particles (Fig. S2). The experimental profile of the mixed sample differs from the simple sum of the intensity contributions of the two components, indicating the occurrence of interactions between the NPs and mucin.

The model of this mixed system is not simple, as the system is likely to be quite inhomogeneous. The intensity profiles of mucin and NPs differ over the entire investigated q range. The intensity of the NPs is significantly lower than that of mucin, except in the q region between 0.1 and 0.7 nm^{-1}, where the NPs display a characteristic modulation that disappears in the mixed system (Fig. S2). This further supports the occurrence of interactions between the NPs and mucin. To obtain some qualitative information on the complexes formed, we hypothesized that a fraction of mucin did not interact with the NPs and described the mixed system as a combination of unbound mucin and mucin–NP complexes. Different increasing amounts of unbound mucin were tested, and we could not exceed 90% unbound mucin. Although this description is quite rough, the analysis suggests that at least approximately 10% of mucin may be associated with the NPs. The corresponding subtracted intensity profiles for all systems are reported in Fig. 3 (right panel). These intensity profiles may provide some indication of the arrangement of the complexes. The intensity modulation at 0.3 nm^{-1}, resulting from the organization of chitosan chains, completely vanishes and the intensity decays indicate a quite compact surface fractals arrangement ($(q) \div q^{-3.2}$ - $q^{-3.6}$). The results suggest that the chitosan chains are entangled with the mucin chains in polydisperse compact clusters with rough surfaces. At distances longer than 200 nm, these compact clustered regions are connected into larger, looser complexes ($(q) \div q^{-1.5}$ - q^{-2}).

Overall, the results indicate that the addition of the antigen did not significantly alter the overall size or structural features of the NPs. Instead, antigen adsorption primarily modified the surface organization: CHIT-MAN NPs adopted a more compact surface structure, while CHIT-LA NPs became slightly looser. Notably, despite this looser surface arrangement, the underlying polymer network of CHIT-LA NPs remains

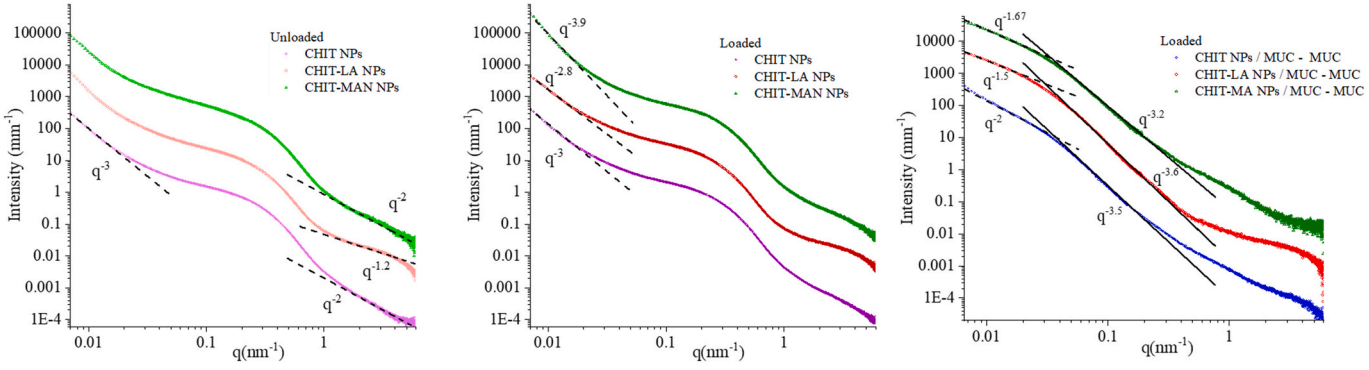


Fig. 3. SAXS intensity profiles for chitosan-based NPs. Left panel: unloaded NPs; central panel: loaded NPs associated with the SARS-CoV-2 antigen; right panel: NPs associated with the SARS-CoV-2 antigen after incubation with mucin after subtraction of an appropriate fraction of the mucin spectrum. Dashed lines represent the intensity decay trends.

relatively rigid. These findings indicate that carbohydrate functionalization can modulate the internal organization of chitosan-based NPs, while antigen adsorption and exposure to mucin can further influence their structural organization.

3.3. Permeability and mucoadhesive behavior of chitosan-based NPs on excised rabbit nasal epithelium

The physicochemical properties of NPs play a critical role in their ability to navigate this complex barrier. In this context, assessing the permeability and mucoadhesive properties of chitosan-based NPs is crucial to optimizing their use in intranasal vaccine formulations [25]. The use of excised rabbit nasal mucosal tissue provides an ideal model for evaluating nasal drug delivery systems. The rabbit nasal septum represents a viable model for evaluating human nasal mucosal barriers, as it is characterized by a thin structure (ranging from 50 μm to 350 μm) covered by a pseudostratified columnar epithelium and exhibits a ciliated respiratory epithelium [26].

For permeability assessment, FITC-labeled CHIT, CHIT-LA, and CHIT-MAN NPs were applied to excised nasal tissue and monitored over time by two-photon microscopy. Different signals can be clearly distinguished: a) the second harmonic generation (SHG) signal associated with collagen, observed at 450 nm (half of the excitation wavelength), b) the fluorescence spectra of FITC in the 500–600 nm spectral region; c) the autofluorescence of the blank mucosa, that was collected prior to applying the formulations, ensuring that any fluorescence attributed to the NPs was not confounded by the natural fluorescence of the tissue itself. Tissue regions with a clearly identifiable collagen SHG signal and suitable mucosal structure were selected, and the same acquisition settings were maintained throughout the experiment.

As expected for *ex vivo* biological tissue, differences in tissue structure and initial fluorescence intensity were observed between representative samples at T0 (Fig. 4A). Although the mucosal discs were prepared using the same procedure and standardized dimensions, intrinsic differences in tissue structure and in the initial distribution of the applied formulations may contribute to variations in the observed fluorescence signal. Therefore, absolute fluorescence intensity at T0 was not used to compare permeability between formulations. Instead, changes in the FITC fluorescence signal were monitored over time at the same location and approximately the same depth within each tissue sample, allowing the progression of NP-associated fluorescence into the tissue to be assessed. The data showed that CHIT NPs did not exhibit an appreciable increase in fluorescence intensity over time, suggesting limited transport of FITC to the monitored tissue depth, whereas CHIT-LA and CHIT-MAN NPs exhibited an increase in fluorescence intensity, consistent with greater transport of the FITC-labeled NPs into the tissue (Fig. 4B–D). This difference may be related to the ability of carbohydrate-functionalized NPs to interact with cellular components within the mucosal tissue, potentially facilitating their passage through the nasal barrier.

The results observed for CHIT NPs align with findings in the literature. For instance, a study conducted by Giuliani et al. demonstrated that in *ex vivo* transport studies using rabbit nasal mucosa, chitosan showed a limited capacity to enhance the permeation of ribavirin compared to other permeation enhancers such as mannitol and α-cyclodextrin, with less than 10% of the drug crossing the mucosa after 30 min [27]. Moreover, Ejaz et al. investigated chitosan nanocarriers functionalized with different biochemical moieties, including mannose, and reported enhanced permeation of mannose-functionalized nanocarriers compared with their unmodified counterparts in an *ex vivo* rat intestinal model [28]. The authors attributed this effect to the high affinity of mannose for mannose-binding lectins expressed on intestinal epithelial cells. Although these findings were obtained in a different mucosal tissue and experimental model, they are consistent with the greater tissue-associated fluorescence observed for the functionalized NPs in the present study. Overall, the present results indicate that carbohydrate functionalization can influence the transport behavior of chitosan-based NPs in nasal mucosal tissue.

To further evaluate their performance under physiological clearance conditions, mucoadhesion studies were performed by exposing the formulations to continuous washing with SNES to simulate mucociliary clearance. Interestingly, CHIT NPs exhibited the highest mucoadhesive capacity, with over 62% of the particles remaining adhered to the mucosa after 5 min of continuous washing, and more than 25% still present after 30 min (Fig. 4E). This finding is consistent with the strong electrostatic interactions expected between the positively charged chitosan surface and negatively charged mucin glycoproteins, which carry sialic acid and sulfate ester residues [29]. However, CHIT-LA and CHIT-MAN NPs also demonstrated significant mucoadhesion, with approximately 50% of the functionalized NPs remaining adhered after 5 min, and 6% of CHIT-LA NPs and 12% of CHIT-MAN NPs still present after 30 min of washing. Despite these differences in retention percentages, the results were not statistically significant between the different formulations, suggesting that all three types of NPs exhibit comparable mucoadhesive properties under the experimental conditions.

At first glance, lower mucoadhesion might be expected following carbohydrate functionalization due to modification of some chitosan amino groups and the resulting changes in surface chemistry. However, by adjusting the amount of TPP used during NP preparation, particles with comparable surface charge were obtained, which may have contributed to the similar mucoadhesive retention observed across the formulations. Nevertheless, NP–mucin association is not determined exclusively by surface charge and may involve several types of non-covalent interactions, including, but not limited to, hydrogen bonding. Furthermore, carbohydrate functionalization does not necessarily result in complete surface coverage, meaning that some surface-accessible chitosan amino groups may remain available for electrostatic interactions with mucin, while the hydroxyl-rich carbohydrate moieties introduce additional groups capable of participating in hydrogen bonding. The resulting mucoadhesive behavior may therefore reflect the combined contribution of these different surface interactions.

Interestingly, after the 30 min washing, the mucosa was left overnight in SNES, and the FITC fluorescence associated with the NPs was measured the next day. The percentage of retained particles remained unchanged compared with the 30 min measurement, with no detectable further loss of fluorescence. This persistence of the fluorescence signal indicates that the retained NPs remained associated with the mucosal tissue under the conditions tested, with no additional detectable loss during the overnight incubation.

Together, these results highlight the importance of considering the interplay between mucus retention and tissue transport when designing chitosan-based nasal delivery systems. The relationship between these properties is complex, as the interactions that favor retention within the mucus layer may, depending on their nature and strength, also influence particle mobility and access to the underlying tissue. In this context, carbohydrate functionalization offers a means of modifying the surface chemistry of chitosan-based NPs while preserving their interaction with the nasal mucosa, supporting their potential for nasal antigen delivery.

3.4. Carbohydrate functionalization of chitosan NPs enhances permeability and reduces cytotoxicity in a human nasal epithelial cell line

To further explore the permeability and cytotoxicity profiles of our chitosan-based NPs, we transitioned from *ex vivo* rabbit nasal mucosa studies to an *in vitro* nasal epithelial cell model, specifically the RPMI 2650 human nasal cell line. Air–liquid interface (ALI) culture has established RPMI 2650 cells as a reliable model of the nasal epithelium, promoting differentiation into a mucociliary phenotype with mucus production, tight junctions, and relevant transport functions [30]. Furthermore, this model exhibits TEER values and paracellular permeability to markers like FITC that are consistent with *ex vivo* human nasal mucosa [15].

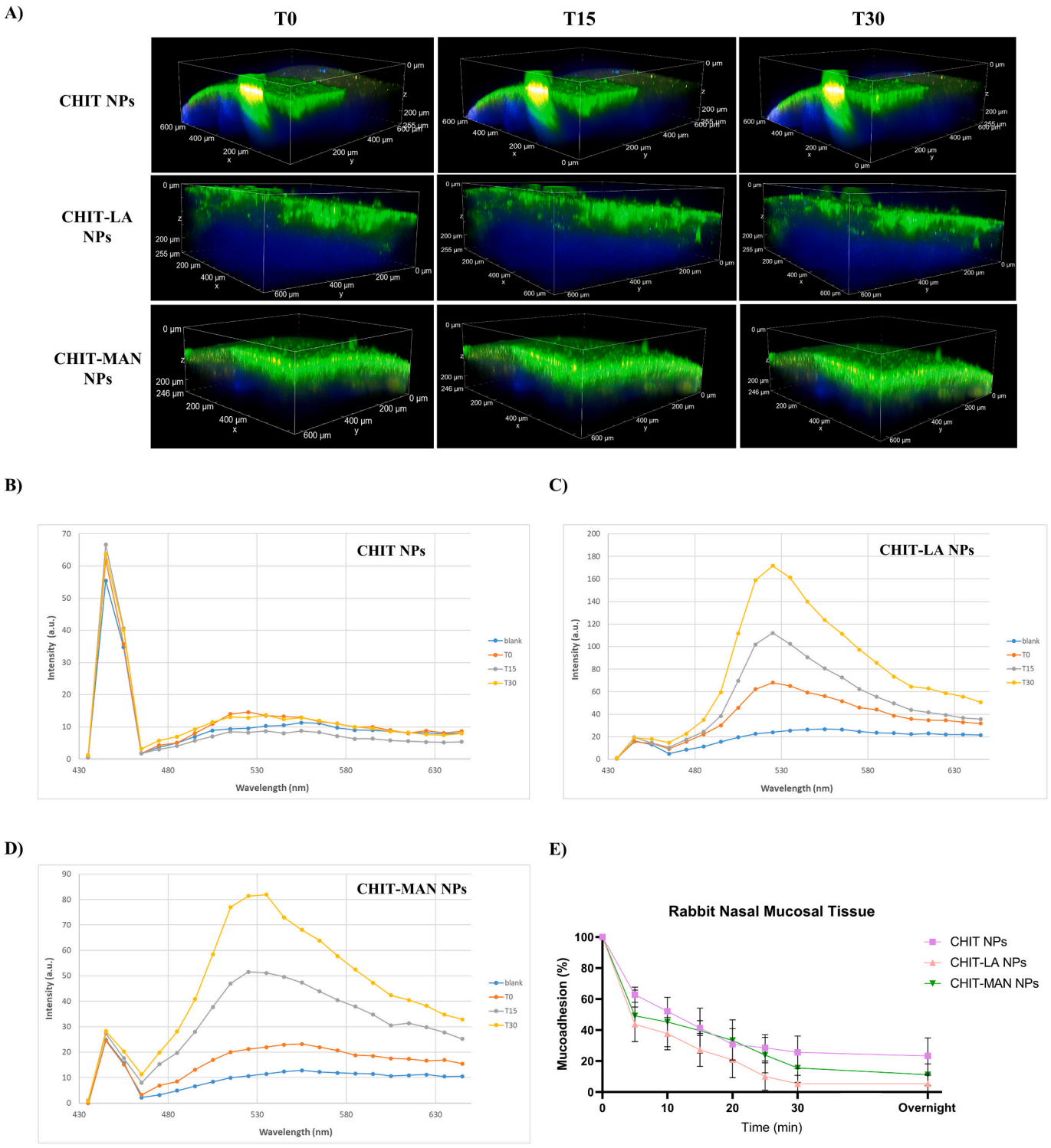


Fig. 4. Permeability and mucoadhesion of FITC-labeled chitosan-based nanoparticles in rabbit nasal mucosal tissue. (A) Representative two-photon microscopy images of FITC-labeled chitosan-based NPs at three timepoints: T0 (immediately after application), T15 (15 min post-application), and T30 (30 min post-application). The green fluorescence corresponds to the FITC-labeled formulations (CHIT NPs, CHIT-LA NPs, and CHIT-MAN NPs), while the blue signal corresponds to the SHG signal associated with collagen in the nasal mucosa. Fluorescence intensity profiles of FITC-labeled chitosan-based NPs at different time points (T0, T15, and T30), measured at the same location on the mucosa. The graphs display the fluorescence spectra for (B) CHIT NPs, (C) CHIT-LA NPs, and (D) CHIT-MAN NPs. Blank mucosa fluorescence (auto-fluorescence control) is also included for comparison. (E) *Ex vivo* mucoadhesion of chitosan-based formulations on rabbit nasal mucosal tissue. The mucosa was flushed with simulated nasal electrolyte solution at a high flow rate for 30 min to mimic physiological conditions. Results are expressed as mean ± SEM ($n = 3$), and statistical differences were analyzed using the Kruskal-Wallis test followed by Dunn's multiple comparisons test with Bonferroni correction.

To establish a safe and effective range of concentrations for permeability studies, we first assessed the cytotoxicity of our NPs using the MTT assay. RPMI 2650 cells were exposed to varying concentrations of functionalized NPs and non-modified chitosan NPs for 20 h. The results, presented in Fig. 5A, revealed that both CHIT-LA and CHIT-MAN NPs exhibited excellent biocompatibility across all tested concentrations. In contrast, CHIT NPs showed a slight reduction in cell viability at the highest tested concentration (2500 μg/mL), dropping below the 70% viability threshold.

The enhanced biocompatibility observed for the functionalized NPs aligns well with previous studies on sugar-based biomaterials. For instance, Höbel et al. explored the modification of poly(ethylene imine) (PEI), a polymer commonly used in DNA and siRNA delivery systems due to its high transfection efficiency but limited by significant cytotoxicity. By functionalizing PEI with sugar molecules such as maltose and maltotriose, they observed a considerable reduction in cytotoxicity while maintaining its transfection efficacy [31]. Similarly, Ejaz et al. developed mannosylated chitosan NPs to enhance their antimicrobial potential against resistant pathogens. Their findings revealed that functionalization with mannose not only improved antimicrobial efficacy but also reduced cytotoxicity compared to unmodified chitosan NPs, as evidenced by hemolytic and protein denaturation studies [32]. The authors associated these effects with the mitigation of strong electrostatic interactions between the cationic polymer and biological membranes, which are known to contribute to cytotoxicity. In our study, carbohydrate functionalization also demonstrated improved biocompatibility compared to non-functionalized chitosan NPs. However, this improvement is unlikely to be explained solely by differences in surface charge, as all three NP formulations exhibited comparable zeta potential values. One possible explanation is that the carbohydrate moieties at the NP surface may provide a steric and hydration barrier that reduces direct interactions between the chitosan backbone and cell membranes. This interpretation is consistent with previous findings showing reduced cytotoxicity and hemolytic effects following carbohydrate functionalization of NPs [33].

To investigate NP transport across the nasal epithelium, FITC-labeled NPs were utilized in permeability studies conducted over 20 h under ALI culture conditions. Fluorescence intensity was measured at various timepoints to evaluate the kinetics of mucosal penetration by the vaccine formulations, as shown in Fig. 5B. FITC alone was included as a control to establish a reference for the permeability of a small, freely soluble molecule. The results demonstrated that FITC alone exhibited the highest permeation, with 2.4 μg crossing the cell monolayer after 20 h. In comparison, permeation for the NPs was lower: 1.8 μg for CHIT-MAN NPs, 1.5 μg for CHIT-LA NPs, and 1.2 μg for CHIT NPs. Despite their higher molecular weight relative to FITC, the functionalized NPs

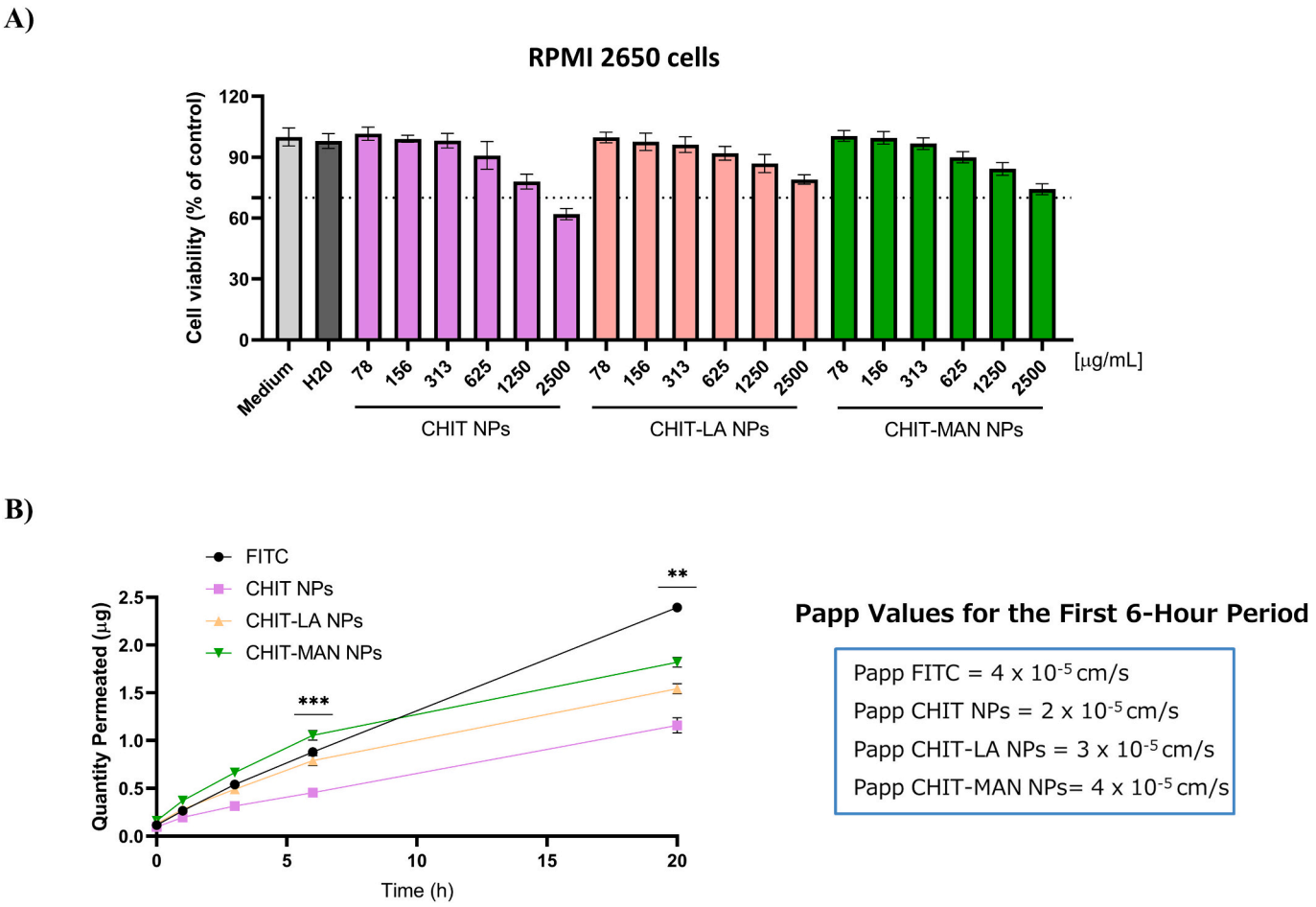


Fig. 5. Evaluation of cytotoxicity and transport of sugar-functionalized and unmodified chitosan nanoparticles across human nasal epithelial cells. (A) *In vitro* cytotoxicity of CHIT, CHIT-LA, and CHIT-MAN NPs on the human nasal epithelial cell line RPMI 2650. Cells were exposed to a range of NP concentrations for 20 h, and cell viability was assessed using MTT assay. (B) Profiles of NP transport across RPMI 2650 cells, showing the cumulative mass of the free fluorophore (FITC) and FITC-labeled CHIT, CHIT-LA, and CHIT-MAN NPs with a maximum measurement period of 20 h. The cumulative mass was determined by interpolating fluorescence values from a calibration curve for each molecule. The apparent permeability coefficient (Papp) of FITC-labeled chitosan-based NPs and the free fluorophore were calculated during the first 6 h of the permeability study. Results are expressed as mean ± SEM ($n = 4$). Statistical analysis was performed using the Kruskal–Wallis test followed by Dunn's multiple comparisons test with Bonferroni correction. Significant differences were observed between CHIT NPs and CHIT-MAN NPs, with significance denoted as follows: $^{**}p < 0.01$ and $^{***}p < 0.001$.

displayed significantly higher permeability than the unmodified CHIT NPs. Notably, CHIT-MAN NPs showed an initial Papp comparable to FITC during the first 6 h, but a plateau effect emerged at later time-points, potentially due to receptor saturation (Fig. 5B). The Papp calculated for our formulations revealed that CHIT NPs had a Papp of 2×10^{-5} cm/s, CHIT-LA NPs reached 3×10^{-5} cm/s, and CHIT-MAN NPs displayed the highest value at 4×10^{-5} cm/s. These values are notably higher than those reported in a related study investigating mannosylated and non-mannosylated chitosan nanocarriers of slightly smaller size (140–160 nm) for oral drug delivery using Caco-2 cells. In that study, mannosylated nanocarriers achieved a Papp of 1.6×10^{-6} cm/s, significantly higher than the non-mannosylated counterparts (9.8×10^{-7} cm/s) [34]. The differences in absolute Papp values between our study and the Caco-2 experiments can largely be attributed to differences in experimental models and conditions. While the Caco-2 cell model simulates the intestinal epithelium, forming a more restrictive barrier due to its specialized tight junctions and intestinal characteristics, our permeability studies were conducted under ALI culture conditions using nasal epithelial cells, which exhibit distinct physiological properties. Nevertheless, both studies emphasize the impact of surface functionalization in enhancing permeability. In the Caco-2 study, the lower permeability of non-mannosylated NPs was attributed to their stronger adhesion to porcine gut mucin, while the greater permeability of mannosylated chitosan NPs was linked to increased hydrophilicity. The authors proposed that increased hydrophilicity reduces non-specific interactions with mucus, thereby facilitating NP mobility and transport across biological barriers [35]. In contrast, in our study, the carbohydrate-functionalized NPs, particularly CHIT-MAN, exhibited greater permeability than the non-functionalized CHIT NPs, despite no significant differences in the measured mucoadhesion. Thus, the increased tissue transport observed here cannot be attributed simply to reduced mucosal retention. Instead, it may reflect other effects of carbohydrate functionalization on NP surface properties, such as surface hydration or interactions with cellular components at the epithelial interface. Importantly, the combination of greater epithelial permeability with maintained mucoadhesive retention suggests that carbohydrate functionalization may modify NP transport without necessarily compromising their interaction with the mucosal surface.

Interestingly, the relationship between permeability and the form of the tested substance (soluble *versus* nanoparticulate) aligns with findings by Sadeghi et al., who examined the effect of various chitosan derivatives on insulin transport across intestinal Caco-2 monolayers. Their study showed that chitosan derivatives in free-soluble form facilitated paracellular transport more effectively than their NP counterparts [36]. Paracellular transport, which allows substances to pass through intercellular spaces *via* diffusion, explains why free-soluble chitosan performed better in their model. Similarly, in our study, free FITC exhibited higher permeability compared to the FITC-labeled chitosan NPs. This difference is expected given the substantially smaller size of FITC and its ability to cross the epithelial barrier without the physicochemical constraints associated with a nanoparticulate carrier. The higher permeability of free FITC should therefore not be interpreted as indicating that greater epithelial permeability is necessarily the primary objective of a NP-based vaccine delivery system. Unlike a small, freely soluble molecule such as FITC, a NP can associate the antigen with a particulate carrier, potentially improving its retention at the mucosal surface and protecting it from the conditions encountered after administration, while also facilitating interactions with cells involved in antigen uptake and presentation [37]. Therefore, the potential benefit of the NP formulations lies not simply in their ability to cross the epithelial barrier, but in their capacity to combine antigen delivery with the physicochemical and biological properties of the carrier.

Before and after the permeability tests, TEER readings tracked epithelial barrier integrity. Chitosan-based NPs caused a small, non-cytotoxic TEER reduction consistent with transient tight junction modulation, whereas FITC alone showed no impact (Fig. S3A). Lysozyme degradation tests confirmed the stability of FITC labeling by revealing little fluorophore release over 20 h (Fig. S3B).

3.5. Carbohydrate-functionalized chitosan NPs drive targeted uptake and M1 activation in human macrophages

Macrophages are important APCs involved in the regulation of innate and adaptive immune responses in mucosal tissues such as NALT. In these environments, macrophages frequently exhibit an M2-like phenotype associated with immune tolerance, which can limit effective immune activation following mucosal vaccination [38]. Therefore, strategies capable of enhancing macrophage uptake and promoting a shift toward a more pro-inflammatory phenotype may improve the immunostimulatory potential of intranasal vaccine delivery systems. In this study, monocytes differentiated with M-CSF were used as an M2-like macrophage model to evaluate the interaction of carbohydrate-functionalized chitosan NPs with macrophages.

To investigate NP internalization, macrophages were incubated with FITC-labeled CHIT, CHIT-LA, and CHIT-MAN NPs for 4 h and uptake was evaluated by flow cytometry. Results revealed robust internalization across all NP formulations compared to the control group, which included cells treated with free FITC or left untreated (iMs) (Fig. 6A). Among the tested formulations, CHIT-LA and CHIT-MAN NPs demonstrated the highest levels of cellular uptake, showing statistically significant increases over the FITC control. Specifically, approximately 80% of macrophages were FITC-positive following incubation with CHIT-LA NPs, while CHIT-MAN NPs resulted in an even higher proportion of FITC-positive cells (87%). By contrast, unmodified CHIT NPs yielded an average of 68% FITC-positive macrophages, which was lower than that observed for the functionalized nanoparticles but still substantial.

Given the presence of galactose and mannose residues on CHIT-LA and CHIT-MAN NPs, respectively, receptor blocking experiments were performed to investigate whether uptake occurred through lectin-mediated interactions. Macrophages were pre-incubated with anti-MGL or anti-MR antibodies prior to NP exposure. Parallel experiments without antibody pre-treatment served as controls to assess baseline uptake. The results revealed a significant reduction in the internalization of functionalized NPs in the presence of blocking antibodies, strongly suggesting a receptor-dependent uptake mechanism (Fig. 6B). Specifically, CHIT-LA NP internalization decreased by a factor of 2.2 when cells were pre-treated with MGL antibodies, while CHIT-MAN NP internalization decreased by a more pronounced factor of 2.9 in the presence of MR antibodies. In contrast, the uptake of unmodified CHIT NPs remained unaffected, regardless of antibody pre-treatment, indicating that their internalization was not dependent on MR or MGL binding. To further validate these findings, confocal microscopy was employed to visualize the localization of FITC-labeled NPs in macrophages after 4 h of incubation (Fig. 6C). A strong green fluorescence signal was observed within cells treated with chitosan-based NPs, confirming successful internalization of the NPs. The fluorescence was clearly localized within the cell boundaries, as evidenced by the co-staining of the nuclei and cell membranes, indicating that the NPs had entered the cytoplasm rather than merely adhering to the cell surface. In contrast, cells treated with free FITC showed markedly lower levels of fluorescence, consistent with the limited uptake observed in the flow cytometry data.

Following the uptake studies, the immunomodulatory effects of the formulations were evaluated by measuring ROS and NO production, both associated with macrophage activation. As shown in Fig. 7A, CHIT-MAN NPs uniquely triggered a significant increase in ROS production, resulting in a 1.5-fold increase in mean fluorescence intensity compared to untreated controls. By contrast, neither CHIT nor CHIT-LA NPs elicited ROS generation under the same conditions. Interestingly, the positive control, LPS, did not induce ROS production during the 2 h incubation, likely due to its requirement for a longer activation period.

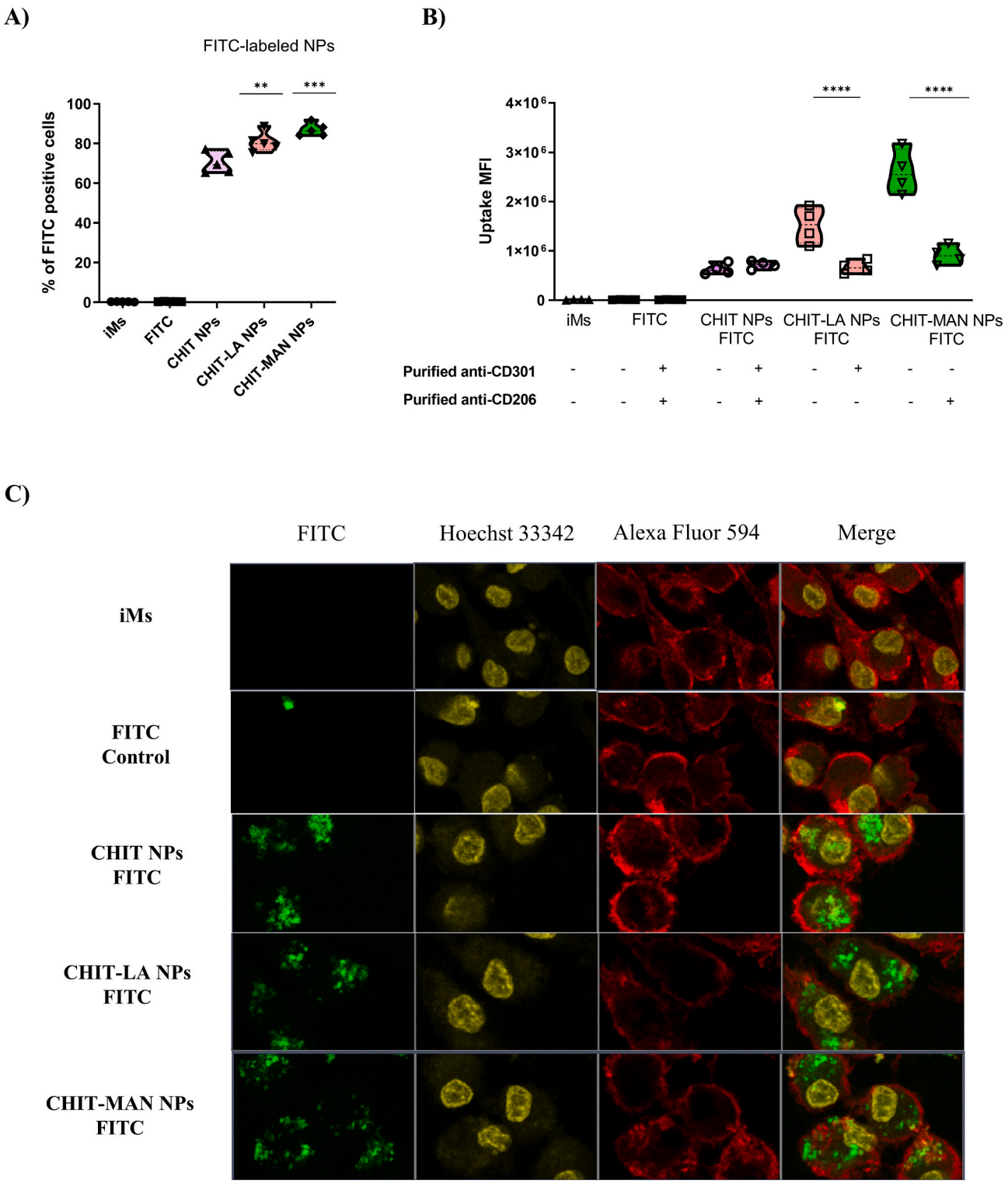


Fig. 6. Evaluation of internalization of carbohydrate-functionalized and unmodified nanoparticles in human monocyte-derived macrophages. (A) The uptake of NPs by macrophages was quantified following a 4 h incubation with FITC-conjugated chitosan-based NPs, with the results expressed as the percentage of FITC-positive cells, as determined by flow cytometry. (B) To assess receptor-mediated internalization, macrophages were pre-treated with purified antibodies against the MR or MGL for 1 h to block receptor-specific uptake before exposure to the particles. Each data point represents an independent donor. Statistical analysis was performed using the Kruskal-Wallis test followed by Dunn's multiple comparisons test with Bonferroni correction, with significance denoted as follows: $^{*}p < 0.05$, $^{**}p < 0.01$, $^{***}p < 0.001$, and $^{****}p < 0.0001$. (C) Representative confocal microscopy images showing NP uptake by macrophages. FITC-labeled particles are shown in green, nuclei are stained with Hoechst 33342 (yellow), and cell membranes are labeled with Alexa Fluor 594 WGA (red). Stacked images compare untreated macrophages (iMs) with cells exposed to FITC alone and those treated with functionalized and unmodified chitosan NPs, providing a visual representation of particle internalization and localization.

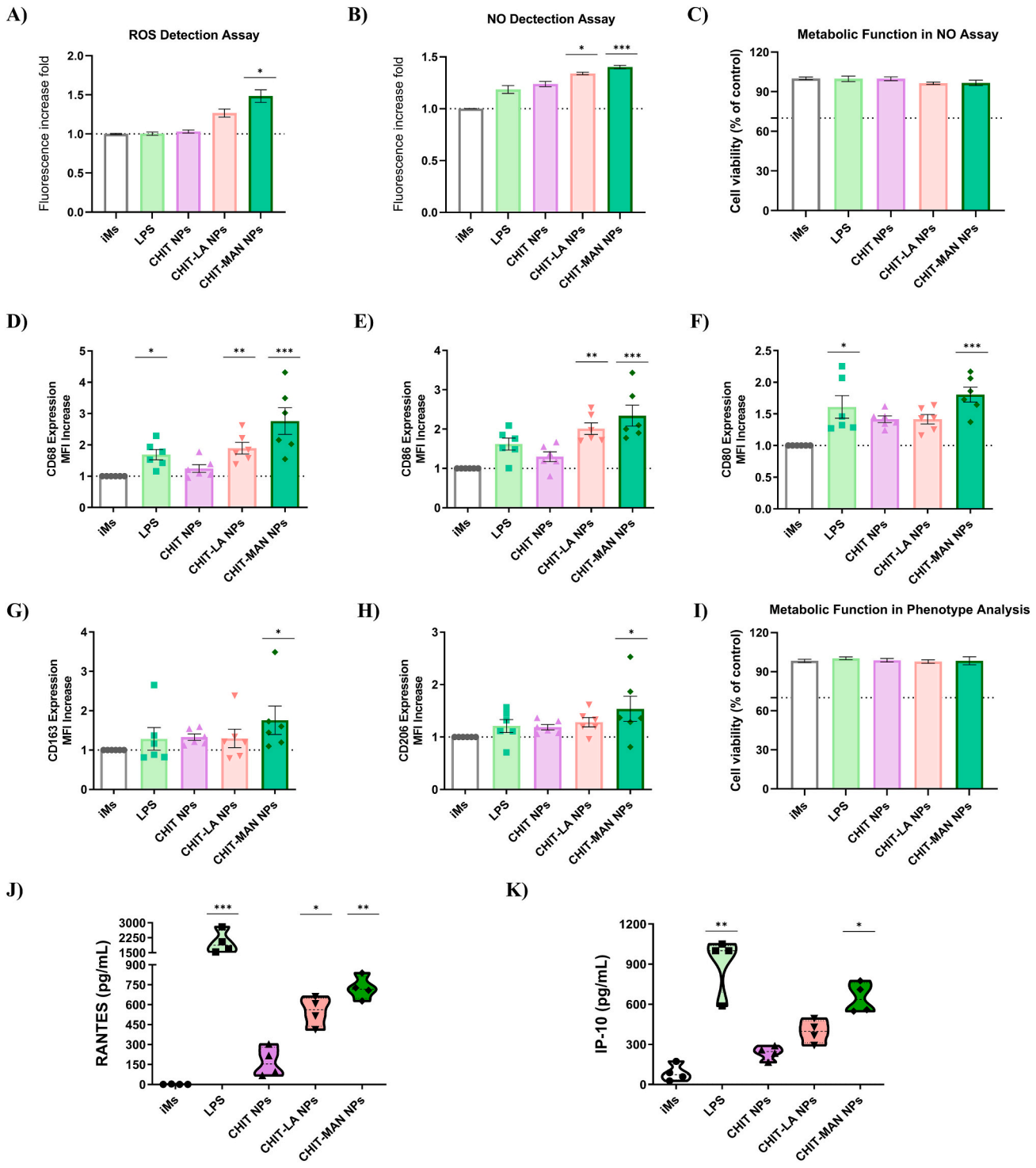


Fig. 7. Functional and phenotypic activation of human monocyte-derived macrophages upon exposure to carbohydrate-functionalized chitosan-based vaccine formulations. (A) Macrophage production of reactive oxygen species (ROS) was measured after a 2 h incubation with NPs (5 μg/mL). Lipopolysaccharide (LPS, 1 μg/mL) was used as a positive control, while unstimulated cells were included as a negative control. (B) Nitric oxide (NO) levels were quantified after 24 h of exposure to the NP formulations using a fluorescence probe. LPS served as the positive control. The fluorescence fold increase for both ROS and NO was calculated by comparing the mean fluorescence intensity (MFI) of the stimulated samples with the negative control. (C) Cell viability was confirmed under the same conditions as in (B) using the resazurin assay ($n = 4$). The expression of key macrophage surface markers was evaluated 24 h after stimulation. Flow cytometric analysis was used to measure the MFI increase for CD68 (D), CD86 (E), CD80 (F), CD163 (G), and CD206 (H) in cells treated with chitosan-based formulations or LPS (1 μg/mL), with untreated cells as controls. (I) The viability of macrophages during surface marker expression analysis was confirmed using the resazurin assay. Secretion of chemokines by macrophages was measured in the cell culture supernatants after 24 h of stimulation with LPS, CHIT, CHIT-LA, or CHIT-MAN NPs. The levels of RANTES (J) and IP-10 (K) were quantified. Statistical differences were determined using the Kruskal-Wallis test followed by Dunn's multiple comparisons test with Bonferroni correction, with significance indicated relative to the unstimulated control as follows: $*p < 0.05$, $**p < 0.01$, and $***p < 0.001$.

The production of NO provided additional insights into the immunostimulatory potential of the NPs. Both CHIT-LA and CHIT-MAN NPs significantly increased NO levels, with fold increases of 1.35 and 1.4, respectively, compared to untreated cells (Fig. 7B). These results suggest that carbohydrate-functionalized chitosan NPs are capable of modulating macrophage activation, with CHIT-MAN NPs exhibiting a prominent pro-inflammatory activation profile among the formulations tested. Importantly, these immunostimulatory responses occurred without compromising cell viability, as confirmed by the resazurin assay (Fig. 7C).

Following the observed effects of carbohydrate-functionalized chitosan NPs on ROS and NO production, we sought to determine whether these formulations could influence the phenotypic polarization of macrophages by assessing the expression of specific surface markers associated with M1 and M2 states. The gating strategy used for macrophage phenotypic analysis is shown in Supplementary Fig. S4. Human monocytes differentiated into macrophages using M-CSF were employed as the cellular model, as this differentiation protocol yields macrophages that predominantly exhibit an M2-like phenotype. These cells are marked by high expression of scavenger receptors such as CD206 and CD163, which reflect their tissue repair and anti-inflammatory functions, along with comparatively low levels of M1-associated markers like CD86, CD80, and HLA-DR, which are crucial for antigen presentation and lymphocyte co-stimulation [39]. CD68, on the other hand, is a widely recognized general macrophage marker but has also been linked to inflammatory processes. Under conditions of heightened immune activation, such as exposure to oxidized low-density lipoprotein, CD68 expression increases, making it a useful indicator of an M1-like inflammatory state when elevated beyond basal levels [40]. Upon stimulation with the chitosan-based NPs, notable shifts in macrophage surface marker expression were observed, reflecting potential phenotypic modulation. Both CHIT-LA and CHIT-MAN NPs significantly upregulated markers associated with M1 polarization, including CD68, CD86, and CD80 (Fig. 7D-F). Among these, CHIT-MAN NPs showed the highest MFI increases, with 2.8, 2.4, and 1.8-fold increases for CD68, CD86, and CD80, respectively. These responses were numerically higher than those observed for the LPS positive control under the conditions tested. Similarly, CHIT-LA NPs elicited significant MFI increases of 1.9 and 2.1-fold for CD68 and CD86, respectively, when compared to untreated macrophages. Interestingly, CHIT-MAN NPs also induced modest increases in the expression of the M2-associated markers CD163 and CD206 (Fig. 7G-H). However, these responses were more variable than those observed for the M1-associated markers and were largely driven by one particularly responsive donor out of the six tested. Notably, CD206 corresponds to the macrophage MR, which represents a proposed recognition pathway for the mannosylated CHIT-MAN formulation. Therefore, modulation of CD206 expression is not necessarily inconsistent with the observed pro-inflammatory activation profile. In contrast, the unmodified CHIT NPs did not elicit significant changes in the expression of any of the surface markers evaluated, underscoring the critical role of functionalization in modulating macrophage phenotype. Importantly, to rule out cytotoxicity as a confounding factor, cell viability was assessed under all experimental conditions. None of the formulations, including CHIT-LA and CHIT-MAN NPs, had any adverse effects on cellular viability, as confirmed by the resazurin assay (Fig. 7I).

Chemokines play key roles in regulating immune cell recruitment and activation. Among them, IP-10 (CXCL10) and RANTES (CCL5) are important inflammatory mediators associated with pro-inflammatory and Th1-type immune responses. Evaluating their expression provides insight into whether the NPs promote an activated immune environment. The findings demonstrated that among the tested formulations, CHIT-MAN NPs were the most effective in promoting an activated macrophage phenotype, as evidenced by a significant increase in the secretion of the inflammatory chemokines RANTES and IP-10 compared to untreated controls (Fig. 7J-K). Specifically, CHIT-MAN NPs induced the secretion of approximately 710 pg/mL of RANTES and 650 pg/mL of IP-10, whereas untreated cells exhibited baseline levels of around 2 pg/mL and 80 pg/mL, respectively. Although CHIT-LA NPs did not induce a statistically significant increase in IP-10 levels, they did significantly elevate RANTES secretion to approximately 530 pg/mL compared to iMs. In contrast, CHIT NPs did not induce any discernible changes in the secretion of either chemokine. As expected, the positive control, LPS, robustly stimulated the secretion of both chemokines, demonstrating the pro-inflammatory potential of this classical activator of macrophages.

IL-6 secretion was also evaluated as a functional indicator of potential endotoxin-related effects. None of the formulations induced detectable IL-6 secretion, whereas LPS elicited a marked response (Fig. S5), providing functional evidence consistent with the absence of biologically relevant endotoxin contamination under the conditions tested. This is in agreement with the apyrogenic procedures used for NP preparation.

The use of carbohydrates to target macrophage receptors is a well-established strategy. For instance, Su et al. designed glycosylated NPs functionalized with D-galactopyranoside, α-D-mannopyranoside, and L-fucopyranoside to specifically bind macrophage surface receptors such as MGL and MR. They demonstrated receptor-mediated internalization through blocking antibody experiments in RAW 264.7 cells, showing significant inhibition of uptake in the presence of the respective antibodies. Importantly, these glycosylated NPs successfully repolarized RAW 264.7 macrophages from an M2 to an M1 phenotype, with increased CD86 expression and elevated IL-12 levels [41]. Interestingly, formulations targeting the MR exhibited a stronger pro-inflammatory potential than those targeting the MGL, aligning with our findings that MR-targeting NPs can induce robust macrophage activation. Similarly, Nascimento et al. developed a mannosylated budesonide palmitate nanoprodrug, which demonstrated significantly higher internalization into macrophages compared to PEGylated NPs. This uptake was confirmed to be MR-mediated through inhibition studies using mannan, a known MR ligand [42]. Other studies have further validated the potential of mannosylated NPs for macrophage reprogramming and immune activation. Ye et al. compared bare liposomes, PEGylated liposomes, and mannosylated liposomes, finding that the mannosylated liposomes effectively polarized M2 macrophages to an M1 phenotype by increasing the CD86/CD206 expression ratio *via* MR internalization. This polarization resulted in significant inhibition of glioma tumor growth in a G422 model [43]. In parallel, galactose-functionalized NPs have also shown promise. Wu et al. designed galactosylated low-density lipoprotein NPs to target Kupffer cells in the liver, leveraging MGL-mediated internalization to enhance antigen-specific T-cell responses. Their experiments demonstrated receptor-specific uptake in MGL-expressing ANA1 macrophage-like cells but not in NIH3T3 fibroblasts, which lack MGL expression [44].

In our study, functionalized NPs, particularly CHIT-MAN NPs, effectively induced ROS and NO production in macrophages. This aligns with reports linking M1 polarization to key transcription factors, including nuclear factor kappa B (NF-κB), signal transducer and activator of transcription 1 (STAT1), activator protein 1 (AP-1), and interferon regulatory factor 5 (IRF5). For instance, ROS activates the NF-κB pathway by inhibiting the phosphorylation of IκBα, leading to its ubiquitination and degradation. This degradation enables the nuclear translocation of NF-κB, which in turn drives the transcription of pro-inflammatory genes such as those encoding iNOS, IL-12, TNF-α, IP-10, and RANTES—hallmarks of the M1 phenotype [45]. The intertwined relationship between ROS and NO production provides additional insight into our findings. ROS can activate molecules such as JNK and p38 MAPK, which synergize with transcription factors like NF-κB, STAT1, AP-1, and IRF5 to amplify M1-related gene expression [46]. Furthermore, ROS-driven NF-κB activation directly upregulates iNOS transcription, leading to enhance NO synthesis. Although these pathways were not directly investigated in the present study, the observed ROS and NO production is consistent with their potential involvement in the pro-inflammatory macrophage responses induced by the

carbohydrate-functionalized NPs.

3.6. Enhanced antibody-mediated protection against SARS-CoV-2 achieved via intranasal administration of carbohydrate-functionalized NPs

To evaluate the immunological performance of the developed formulations, a murine intranasal vaccination study was conducted using chitosan-based NPs (CHIT, CHIT-LA, and CHIT-MAN) and soluble antigen as control. The protocol consisted of three intranasal administrations given at two-week intervals. Each dose comprised 500 μg of chitosan-based NPs with 10 μg of the S protein from the Omicron variant adsorbed to their surface. Adsorption of the antigen was performed after NP formation to ensure the structural integrity and functionality of the S protein. This approach was taken to avoid potential antigen degradation during the high-speed homogenization process used in NP synthesis, thereby preserving its stability and immunogenicity for optimal vaccine performance.

The humoral immune response induced by vaccination was evaluated by quantifying serum anti-SARS-CoV-2 IgG titers. All vaccine formulations elicited a 100% response rate in mice, as all animals produced detectable levels of anti-SARS-CoV-2 IgG antibodies. Notably, while the group vaccinated with the antigen alone also achieved a full response rate, it exhibited significantly lower antibody titers compared to the chitosan-based groups (Fig. 8A). This highlights the critical role of the chitosan-based NPs as adjuvants in enhancing the humoral immune response. Analysis of the IgG subtypes revealed distinct patterns of immune response across the vaccine groups. The chitosan-based formulations predominantly stimulated IgG1 production, accompanied by evident levels of IgG2c and IgG3 antibodies, indicating the induction of a mixed IgG subclass response with a Th2-skewed profile. Notably, this diverse antibody profile was consistent across all chitosan formulations, suggesting that the carbohydrate functionalization did not substantially alter the IgG subclass distribution. In contrast, the group vaccinated with the antigen alone exhibited a markedly skewed response, with IgG1 being the predominant antibody produced. Specifically, 4 out of 5 mice in this group generated IgG1, while only 1 out of 5 produced IgG2c, and none produced IgG3, indicating a less balanced immune response (Fig. 8A). Importantly, no anti-SARS-CoV-2 IgE antibodies were detected in any group, underscoring the safety of the vaccine formulations by demonstrating the absence of allergic or hypersensitivity reactions.

While serological tests have proven to be highly sensitive and specific in identifying the presence of IgG antibodies targeting SARS-CoV-2, the detection of such antibodies does not necessarily correspond to the existence of neutralizing antibodies (Nab) [47]. Nab are a subset of antibodies that specifically target the virus, preventing it from entering host cells and arresting its replicative capacity. These antibodies are critical in conferring protective immunity, as they directly block the interaction between the viral S protein and the ACE2 receptor, which is

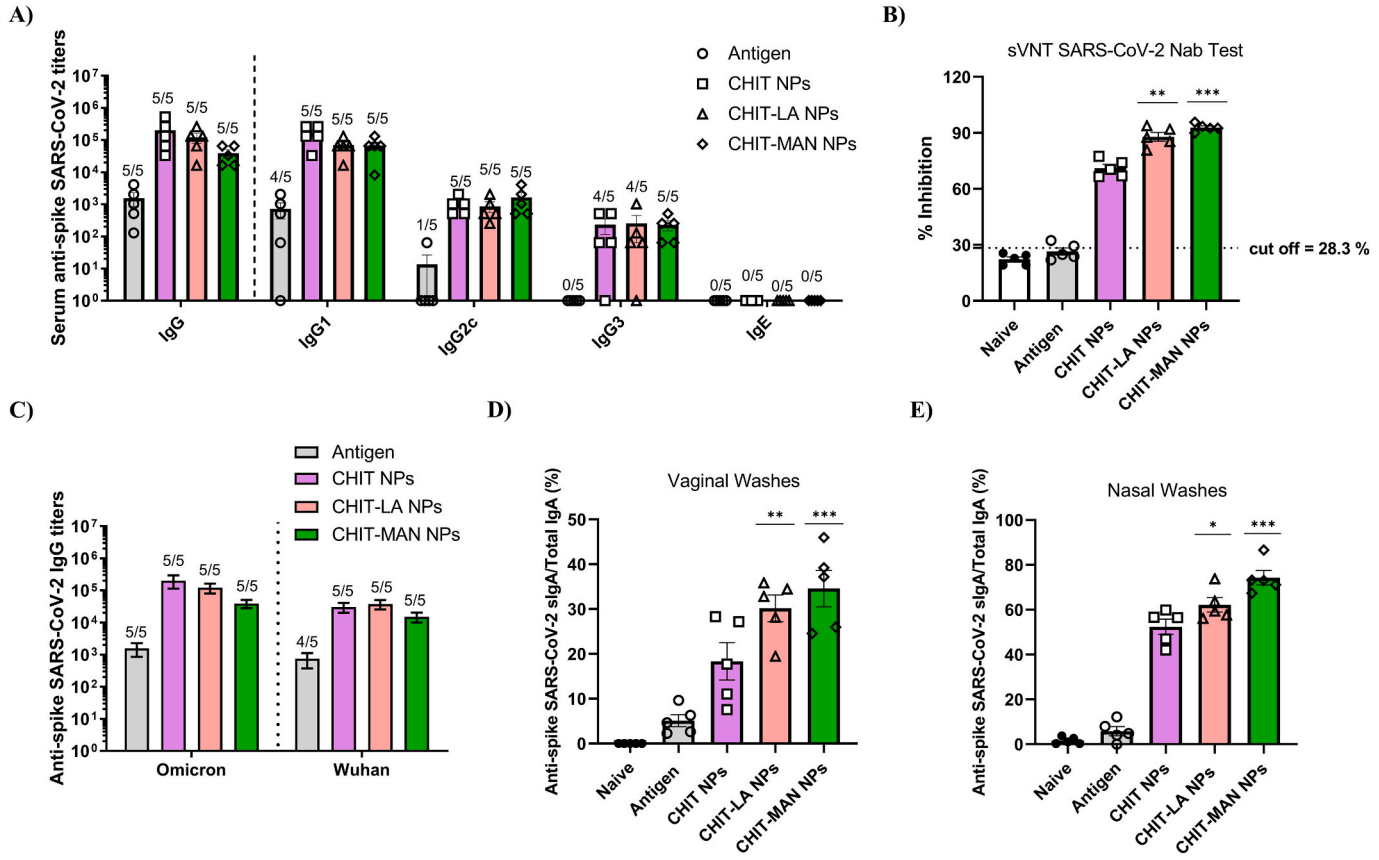


Fig. 8. Humoral (systemic and mucosal) immune responses induced by intranasal vaccination with chitosan-based protein-subunit formulations against SARS-CoV-2. (A) Systemic humoral responses were evaluated by measuring total SARS-CoV-2-specific IgG levels in serum from individual mice 14 days after the third vaccine dose. Subclass analyses of IgG1, IgG2c, IgG3, and IgE were performed on day 42, with titers defined as the highest plasma dilution producing absorbance values at least twice those of non-immune plasma controls. (B) Neutralizing antibody activity was determined in sera from vaccinated and unvaccinated (naive) mice at the study endpoint. ACE2-binding inhibition was quantified using a surrogate virus neutralization test, with the dotted line representing the inhibition threshold (28.3%). (C) The cross-reactivity of serum IgG titers was assessed against both the Omicron and Wuhan SARS-CoV-2 variants to evaluate the extent of the systemic immune response. Mucosal immune responses were analyzed by quantifying secretory IgA (sIgA) in vaginal (D) and nasal (E) wash samples collected on day 42. Results are expressed as the ratio of SARS-CoV-2-specific sIgA to total IgA for all experimental groups. All data are presented as mean ± SEM ($n = 5$). Statistical significance was determined using the Kruskal-Wallis test followed by Dunn's multiple comparisons test with Bonferroni correction, with differences compared to the naive group indicated as $*p < 0.05$, $**p < 0.01$, and $***p < 0.001$.

essential for viral entry. To measure Nab, the SARS-CoV-2 Surrogate Virus Neutralization Test (sVNT) is frequently employed. Evidence shows that higher levels of Nab are strongly associated with reduced risk of infection and symptomatic disease, making the sVNT a valuable tool for assessing the protective potential of vaccines [48]. As shown in Fig. 8B, all mice vaccinated with chitosan-based formulations demonstrated significant neutralizing activity, with ACE2-binding inhibition percentages well above the established positive threshold. While the unmodified CHIT NPs demonstrated moderate neutralizing activity (~71% inhibition), the functionalized NPs, CHIT-LA and CHIT-MAN, achieved significantly higher inhibition percentages (88% and 93%, respectively), indicating enhanced neutralizing activity despite exhibiting comparable IgG titers in the earlier assay. In contrast, only 1 out of 5 mice in the antigen-only group generated a neutralizing antibody response, and this response was borderline with the threshold. These findings suggest that functionalized chitosan-based NPs may provide an enhanced capacity to elicit neutralizing antibodies compared to unmodified NPs or antigen alone.

Since the onset of the COVID-19 pandemic, the SARS-CoV-2 virus has undergone significant mutations, leading to the emergence of multiple variants. These evolving strains, including the antigenically distinct and highly transmissible Omicron variant, have contributed to successive waves of infections and raised concerns about immune escape. As the virus mutates, new variants may partially evade immunity generated by previous infections or vaccinations, increasing the risk of breakthrough infections and re-infections [49]. To assess the broader protective potential of our vaccine, we measured serum IgG titers against both the Omicron variant used in the vaccine and the ancestral Wuhan strain. Vaccines capable of inducing cross-reactive antibodies could mitigate the need for frequent updates to address emerging variants, thus improving long-term immunity and pandemic preparedness. As depicted in Fig. 8C, all mice inoculated with chitosan-based vaccine formulations demonstrated measurable IgG antibody titers against the Wuhan viral strain, though these were reduced in comparison to the Omicron-specific immune response. In contrast, in the antigen-only group, 1 out of 5 mice did not show detectable IgG specific to the Wuhan strain. Despite this, a strong correlation between the antibody responses to both the Omicron and Wuhan variants was observed, suggesting that the chitosan-based formulations elicited a robust, cross-reactive immune response.

To assess mucosal immunity, antigen-specific anti-SARS-CoV-2 sIgA levels were measured in nasal and vaginal washes on day 42 and normalized to total IgA concentrations for reliable comparisons (Fig. 8D and E). The results revealed that all chitosan-based NPs elicited a higher specific IgA/total IgA ratio compared to both control groups. In vaginal washes, the IgA ratios were 18%, 30%, and 35% for CHIT, CHIT-LA, and CHIT-MAN NPs, respectively, whereas the antigen-only group exhibited a ratio of 5%, and naive mice presented ratios below 1% (Fig. 8D). Similarly, in nasal washes, the IgA ratios were 52%, 62%, and 74% for CHIT, CHIT-LA, and CHIT-MAN NPs, respectively, compared to 6% in the antigen-only group and 1% in naive mice (Fig. 8E). These findings underscore the ability of the chitosan-based formulations, particularly the functionalized NPs, to induce robust mucosal immune responses.

Unlike traditional parenteral vaccines, which typically elicit poor mucosal immunity, intranasal vaccination leverages the programming of lymphocytes for mucosa-specific homing. Antigen-primed cells in the NALT acquire chemokine receptors and integrins, such as CCR10 and α4β1, that enable them to home to barrier tissues, including both the respiratory and genitourinary tracts [50]. This tissue-specific homing capability allows intranasal vaccination to establish humoral responses at multiple mucosal sites. This ability is particularly relevant for combating pathogens that exploit mucosal barriers, such as sexually transmitted viruses like hepatitis B virus (HBV) and HIV. For example, Debin et al. demonstrated that intranasal delivery of cationic NPs based on maltodextrins and loaded with HBsAg, the HBV surface antigen, induced sIgA antibodies in both nasal and vaginal washes, as well as balanced IgG1/IgG2a responses in serum. Mice immunized with the free antigen, by contrast, exhibited no detectable IgA and lower IgG titers [51]. Moreover, Soh et al. developed chitosan NPs loaded with the *Brucella abortus* antigen and observed robust sIgA production in nasal washes, genital secretions, and fecal extracts following intranasal immunization. This response was attributed to the mucoadhesive properties of chitosan, which enhance antigen retention on the mucosal surface, and the spherical structure of the NPs, which increases their residence time. The spherical shape promotes water absorption from mucus, leading to epithelial cell dehydration, separation of tight junctions, and improved antigen uptake [52]. Similarly, the chitosan NPs in our study also demonstrated remarkable mucosal immunogenicity, likely due to similar mechanisms. Furthermore, the functionalized NPs in our formulation produced even higher levels of sIgA, which can be attributed to their targeted ligands enhancing internalization by DCs and macrophages. This observation aligns with findings by Pawar et al., who demonstrated that glycol-modified chitosan NPs achieved superior nasal uptake compared to their non-modified counterparts, leading to an enhanced mucosal immune response [53].

T cells in the NALT exhibit a Th0-type cytokine signature, allowing for rapid differentiation into either Th1 or Th2 cells after nasal antigen exposure. The cytokines secreted by these activated $CD4^+$ T helper cells regulate antibody isotype switching, modulating the balance of the immune response. Th1 cells predominantly drive IgG2c and IgG3 production through the secretion of IFN-γ, essential for antiviral defense and cell-mediated immunity. In contrast, Th2 cells promote IgG1 production, supporting robust humoral responses effective against extracellular pathogens. The relative distribution of these antibody subclasses can therefore provide an indication of the type of immune response elicited, although it should be interpreted together with cellular immune parameters when assessing the overall Th1/Th2 profile. Jiang et al. demonstrated that NPs composed of chitosan and curdlan, used as a mucosal adjuvant for an intranasal H1N1 subunit vaccine, successfully induced both mucosal and systemic immunity. This response was characterized by elevated levels of both IgG1 and IgG2a, indicating the induction of a mixed IgG subclass response and highlighting the immunomodulatory effects of chitosan [54]. Similarly, Sadeghi et al. developed mannosylated chitosan NPs for a subunit vaccine targeting pathogenic bacteria, reporting the induction of multiple IgG subclasses (IgG1, IgG2a, IgG2b and IgG3), which they attributed to enhanced antigen presentation *via* MR targeting [55]. These findings suggest that functionalization of chitosan NPs can enhance their interaction with APCs while retaining the inherent immunostimulatory properties of chitosan.

3.7. Augmented TNF-α production and cytotoxic T cell activity triggered by mannose-modified chitosan NPs

To comprehensively assess the immune response induced by vaccines, it is critical to evaluate immune activity in key tissues such as the spleen and lungs. As a central secondary lymphoid organ, the spleen orchestrates systemic immune responses, particularly by activating lymphocytes. Conversely, the lungs represent a primary site of infection for respiratory pathogens and a critical battleground for localized mucosal immunity. By analyzing immune responses in both the spleen and lungs, researchers can obtain a holistic understanding of how intranasal vaccines elicit protection at both localized and systemic levels.

To evaluate the cellular immune responses induced by intranasal vaccination with chitosan-based NPs, we quantified antigen-specific T cell populations producing key effector cytokines, TNF-α and IFN-γ, using intracellular cytokine staining. Following a 6 h *ex vivo* restimulation with SARS-CoV-2 peptides, the frequencies of cytokine-producing $CD4^+$ and $CD8^+$ T cells were analyzed in both spleen and lung tissues. The gating strategy used for the identification of T lymphocyte subsets is shown in Supplementary Fig. S4. The results demonstrated that mice vaccinated with CHIT-MAN NPs exhibited a

significant increase in SARS-CoV-2–specific TNF-α^+ $CD4^+$ and $CD8^+$ T cells in both spleen and lung tissues compared to unvaccinated controls, highlighting robust immune activation (Fig. 9A-B). Similarly, vaccination with CHIT-LA NPs induced a notable increase in TNF-α^+ $CD4^+$ T cells in the spleen and TNF-α^+ $CD8^+$ T cells in the lungs. Interestingly, while unmodified CHIT NPs failed to generate a significant TNF-α response, they elicited the highest levels of SARS-CoV-2–specific IFN-γ^+ $CD4^+$ and $CD8^+$ T cells in the lungs (Fig. 9C-D). Moreover, CHIT-MAN NPs significantly increased IFN-γ^+ $CD4^+$ T cells in the lungs, whereas CHIT-LA NPs enhanced IFN-γ^+ $CD8^+$ T cells, indicating a degree of cytokine specialization driven by the functionalization. In contrast, all vaccinated groups exhibited comparable frequencies of IFN-γ^+ $CD4^+$ and $CD8^+$ T cells in the spleen relative to unvaccinated controls, suggesting that systemic lymphoid tissues may exhibit more modest cytokine responses to these formulations. These findings demonstrate that functionalized NPs elicit a robust and multifunctional Th1 response in the lungs. This localized response in the respiratory tract highlights the ability of intranasal vaccination to effectively target mucosal immunity, while systemic responses in the spleen remain more subdued.

The cytolytic potential of $CD8^+$ T cells, a critical component of antiviral immunity, was assessed by measuring Granzyme B expression. This enzyme, produced by CTLs, plays a crucial role in eliminating infected or abnormal cells by inducing apoptosis, a programmed cell death mechanism that halts the spread of infection. Intracellular cytokine staining revealed a significant increase in Granzyme B^+ $CD8^+$ T cells in spleen samples from all vaccinated groups with chitosan-based NPs compared to unvaccinated controls (Fig. 9E). Notably, mice vaccinated with CHIT-MAN NPs displayed enhanced Granzyme B expression in both spleen and lung samples after restimulation with SARS-CoV-2 peptides, indicating strong activation of cytotoxic effector functions in these tissues. In contrast, the antigen-only group failed to induce detectable cytolytic activity, as evidenced by the absence of Granzyme B^+ $CD8^+$ T cells in both the spleen and lungs.

SARS-CoV-2 peptide restimulation of spleen and lung cells from mice vaccinated with functionalized chitosan NPs significantly enhanced cell proliferation compared to the naive control group (Fig. 9F). Notably, the CHIT NP vaccine also promoted lymphocyte proliferation in the lungs, which corresponds with the previously observed IFN-γ response. This increased proliferation is a hallmark of effective vaccine-induced immunity, reflecting the clonal expansion of antigen-specific B and T cells. Such expansion is essential for generating a robust pool of effector and memory cells capable of mounting a rapid and effective response upon pathogen re-encounter. Furthermore, the correlation between cytokine production and cell proliferation highlights the critical role of cytokine signaling in driving T cell expansion, underscoring its importance in sustaining a strong immune defense against SARS-CoV-2.

To assess the impact of intranasal vaccination on memory T cell responses, we quantified the proportions of effector memory T cells (T_{EM}) and central memory T cells (T_{CM}) populations in $CD4^+$ and $CD8^+$ T cells from spleen and lung samples following restimulation with SARS-CoV-2 peptides. The data revealed that CHIT-MAN NPs vaccination significantly increased the proportion of T_{EM} cells ($CD44^+CD62L^-$) in both spleen and lungs, indicative of a strong antigen-specific memory response (Fig. 10A-B). For instance, the percentage of $CD44^+CD62L^-$ $CD4^+$ T cells rose from 2.4% in unvaccinated mice to 4.8% in vaccinated mice in the spleen, and from 2.5% to 4.9% in the lungs. A similar trend was observed for $CD8^+$ T cells, with T_{EM} frequencies increasing from 1.4% to 3.1% in the spleen and from 1.5% to 3.8% in the lungs. The CHIT-LA NPs group also showed significant expansion of T_{EM} cells, particularly $CD44^+CD62L^-$ $CD8^+$ T cells in the spleen and lungs and $CD44^+CD62L^-$ $CD4^+$ T cells in the lungs compared to unvaccinated controls. Moreover, vaccination with functionalized chitosan NPs promoted the development of T_{CM} cells ($CD44^+CD62L^+$) in $CD4^+$ T cells within the lungs, with CHIT-MAN NPs elevating the proportion from 13.1% in unvaccinated mice to 15.8% and CHIT-LA NPs increasing it to 16.3% (Fig. 10C). An increase in $CD44^+CD62L^+$ $CD8^+$ T cells was also observed in the CHIT NP group, rising from 7.5% in naive mice to 11.1% in vaccinated animals (Fig. 10D). However, no significant differences in T_{CM} populations were observed in spleen samples across all vaccinated groups compared to unvaccinated controls.

The stronger cellular immune responses elicited by the functionalized NPs were anticipated, considering prior *in vitro* findings. Both CHIT-LA and CHIT-MAN NPs demonstrated enhanced interactions with relevant nasal and immune-cell interfaces, as evidenced by their high permeability across the RPMI 2650 cell model and their ability to modulate macrophage activation toward a pro-inflammatory/M1-like profile. While this enhanced functionality was primarily reflected in the mucosal humoral immune response rather than the systemic one, the cellular immunity data revealed a marked distinction between the functionalized NPs and unmodified chitosan NPs.

Notably, upon restimulation with the same antigen, cells from the CHIT-MAN NPs group exhibited a numerically higher frequency of cytokine-producing cells compared to the CHIT-LA NPs group. This group also demonstrated an enhanced generation of memory T cells, particularly the T_{EM} phenotype, which is critical for rapid localized protection in peripheral tissues like the lungs. These differences may be attributed to the distinct CLR engaged, as the MR likely promotes greater maturation and activation of APCs, enhancing the production of co-stimulatory molecules. These processes result in improved antigen presentation and more robust antigen-specific T and B cell responses. This observation aligns closely with findings reported by Gong et al., who developed PLGA-PEG NPs modified with either mannose or *N*-acetylgalactosamine (a galactose derivative) for targeted delivery to DCs and macrophages. Their study demonstrated that functionalized NPs were more efficiently internalized by APCs due to targeted recognition by MR and MGL, respectively. These functionalized NPs significantly boosted antigen-specific T cell responses, generating high levels of IFN-γ, IL-2, and IL-17A in $CD4^+$ T cells, granzyme B in $CD8^+$ T cells, and increased memory T cell populations [56], similar to the robust cellular immunity observed in our study. Moreover, Lou et al. synthesized virus-mimicking particles (VMPs) using cationic polymers that were either mannosylated or galactosylated and conjugated them to RNA encoding the ovalbumin antigen. Mannosylated VMPs demonstrated a fivefold higher cellular uptake by bone marrow-derived DCs compared to their galactosylated counterparts. Vaccination of mice with mannosylated VMPs elicited significantly stronger ovalbumin-specific CTL responses, which was attributed to enhanced uptake by DCs through MR-mediated endocytosis, followed by efficient MHC I antigen presentation. Interestingly, neither the antigen alone nor the soluble polymer mixed with soluble antigen induced cellular immune responses, excluding any intrinsic adjuvant effect of the polysaccharides [57]. Similarly, in our study, the antigen alone failed to induce any type of cellular immune response, reinforcing the importance of nanocarriers in overcoming barriers to effective immune activation. Furthermore, Du et al. developed a mannose-functionalized pickering emulsion for delivering antigenic peptides as an improved cancer vaccine. By chemically linking mannose residues to PLGA/PLGA-PEG NPs, the authors achieved enhanced antigen-specific cellular immune responses. Their results demonstrated higher levels of IFN-γ-producing cells and increased proliferation of antigen-specific $CD8^+$ T cells in splenic lymphocytes compared to unmodified NPs [58]. Together, these data highlight the critical role of NP functionalization in shaping the magnitude and specificity of vaccine-induced cellular immunity, underscoring the potential of CHIT-MAN NPs as an advanced platform for inducing a strong, targeted, and long-lasting immune response against SARS-CoV-2.

3.8. Functionalized chitosan NPs foster multifaceted SARS-CoV-2-specific cytokine production in spleen and lungs

To gain a comprehensive understanding of the immune mechanisms elicited by functionalized and unmodified chitosan-based subunit vaccines, we assessed cytokine secretion profiles from spleen and lung cells

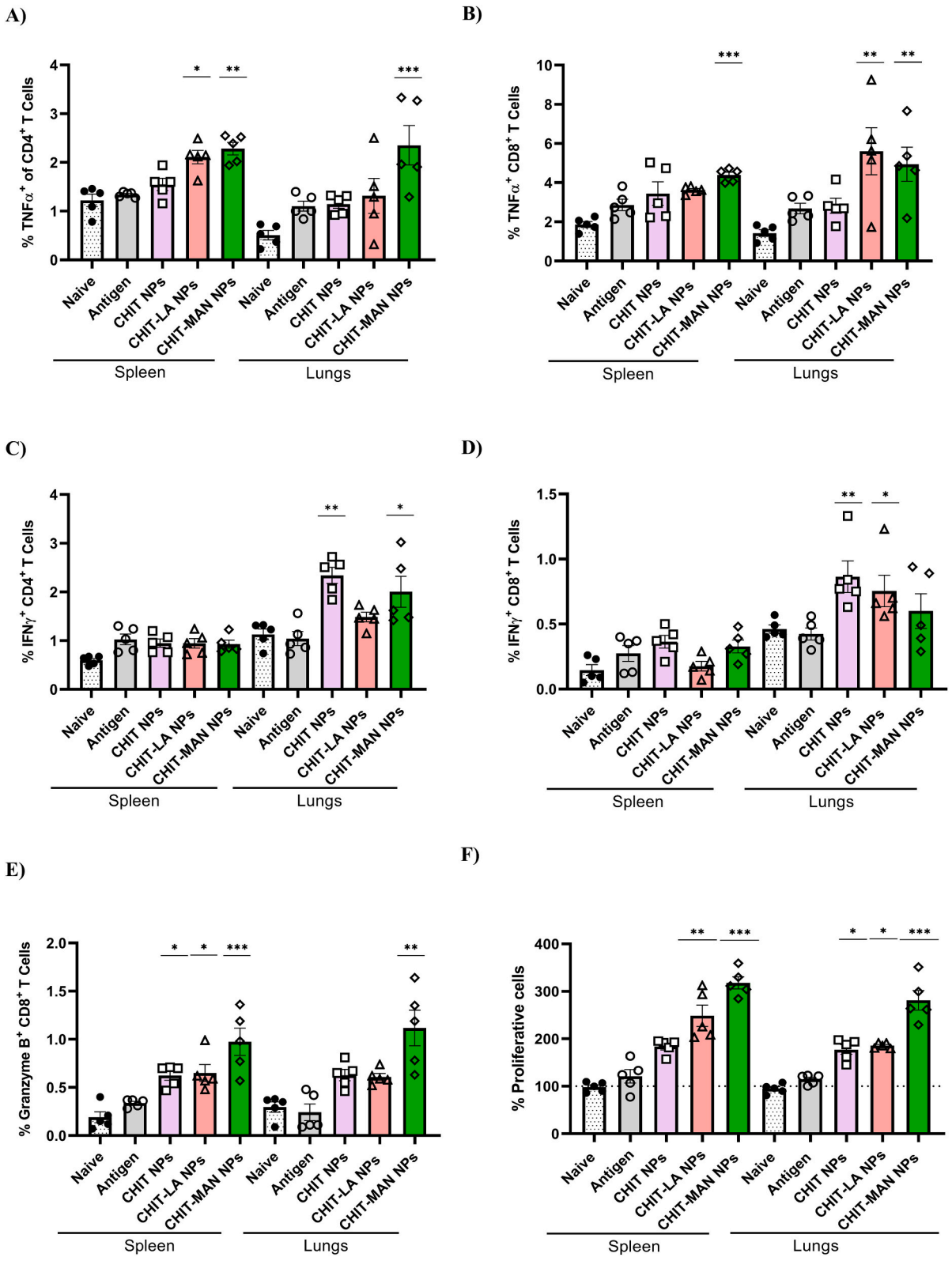


Fig. 9. Intranasal SARS-CoV-2 protein-subunit vaccines induce S protein-specific type 1 cellular immune responses in spleen and lung tissues. Female C57BL/6 mice were immunized intranasally with carbohydrate-functionalized chitosan-based vaccines, receiving three distinct doses. On day 42, spleen and lung tissues were harvested and stimulated *ex vivo* with SARS-CoV-2 S protein peptide pools for 6 h. Immune responses were assessed by flow cytometry. The frequencies of TNF-α-producing (A, B) and IFN-γ-producing (C, D) $CD4^+$ and $CD8^+$ T cells, as well as Granzyme B-expressing (E) $CD8^+$ T cells, were quantified. (F) Cell proliferation was assessed using a BrdU incorporation assay in spleen and lung cells after peptide restimulation to evaluate the expansion of antigen-specific cells. Data are presented as mean ± SEM ($n = 5$). Statistical analysis was performed using the Kruskal-Wallis test followed by Dunn's multiple comparisons test with Bonferroni correction, with significant differences relative to the naive group indicated as $^*p < 0.05$, $^{**}p < 0.01$, and $^{***}p < 0.001$.

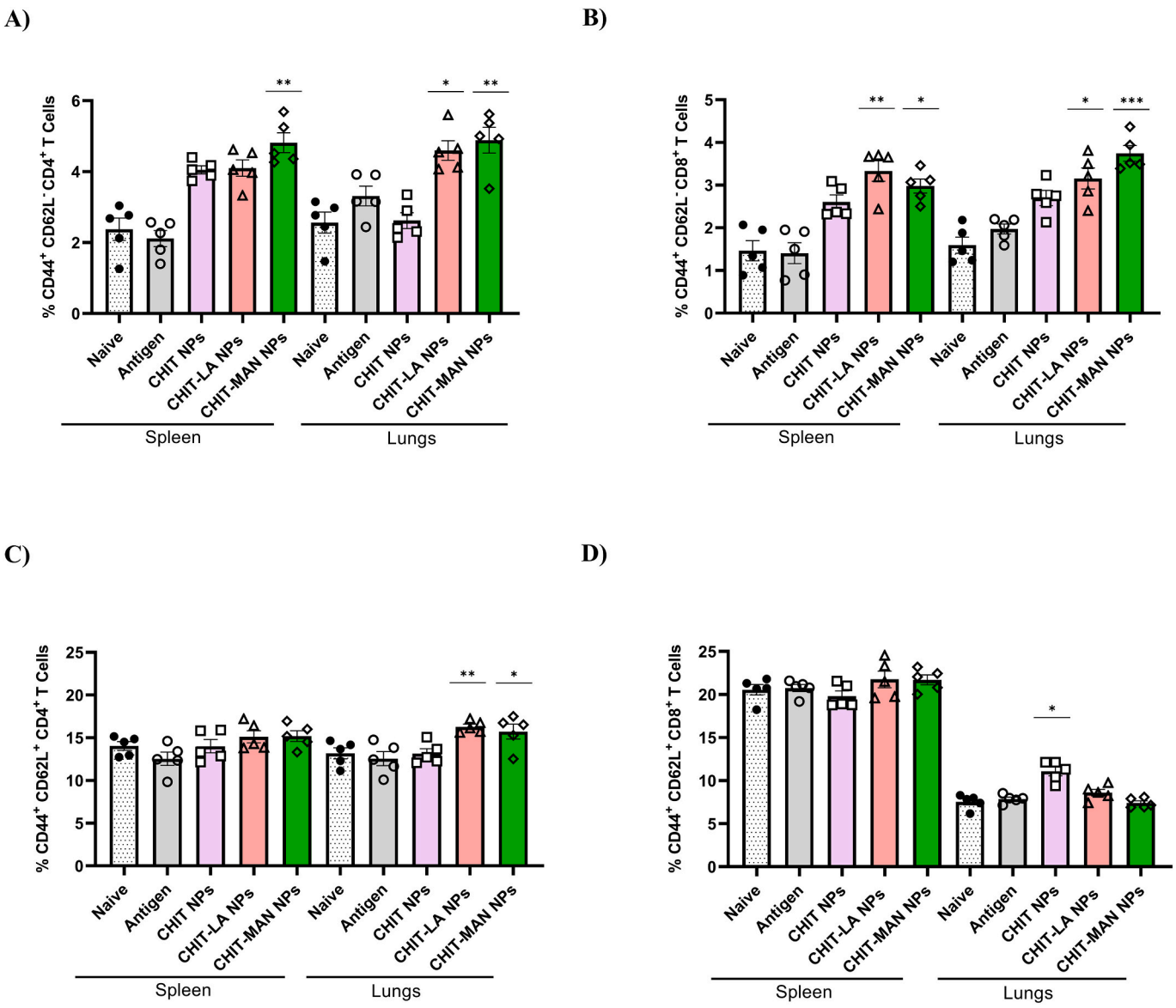


Fig. 10. Memory T cell responses induced by chitosan-based protein-subunit vaccines following SARS-CoV-2 S protein peptide pool restimulation. Effector memory (T_{EM}, $CD44^+CD62L^-$) (A, B) and central memory (T_{CM}, $CD44^+CD62L^+$) (C, D) phenotypes were analyzed in $CD4^+$ and $CD8^+$ T cell populations from spleen and lung tissues after 6 h of *ex vivo* restimulation with SARS-CoV-2 S protein peptide pools. Data are presented as mean ± SEM ($n = 5$). Statistical comparisons were performed using the Kruskal-Wallis test followed by Dunn's multiple comparisons test with Bonferroni correction, with significant differences relative to the control group denoted as $^*p < 0.05$, $^{**}p < 0.01$, and $^{***}p < 0.001$.

following *ex vivo* restimulation with SARS-CoV-2 peptides. Cytokines play pivotal roles in modulating immune responses by influencing the differentiation of naive $CD4^+$ T cells into specialized Th subsets.

To investigate the immunomodulatory effects of the chitosan-based vaccine formulations, we conducted a multiplex analysis targeting 17 cytokines associated with diverse Th pathways. This analysis provided valuable insights into how these formulations shape immune responses. The results, depicted in Fig. 11A, demonstrate that chitosan-based vaccine formulations, both functionalized and unmodified, promoted broad immune activation across nearly all Th subsets, as evidenced by cytokine secretion profiles from restimulated splenic cells. Specifically, splenic lymphocytes from mice vaccinated with functionalized NPs exhibited significantly elevated cytokine levels compared to those from unvaccinated mice or mice immunized intranasally with the antigen alone. Analysis of the heatmap revealed pronounced increases in six key cytokines—IFN-γ, IL-6, IL-18, IL-5, IL-17A, and IL-22—indicating a Th1-, Th2-, and Th17-skewed immune response. The pronounced IL-17A and IL-22 responses observed with CHIT-MAN NPs are particularly relevant in the context of mucosal vaccination, as these cytokines are associated with immune responses at epithelial barriers [59]. In terms of the Th1 response, CHIT-LA NPs significantly increased GM-CSF and IL-2 secretion, whereas CHIT-MAN NPs induced a broader cytokine profile, elevating GM-CSF, IFN-γ, IL-2, IL-6, IL-18, and TNF-α in splenic cell supernatants (Fig. 11B). For the Th2 response, both functionalized chitosan formulations induced substantial increases in IL-5 and IL-13 secretion, with nearly 50-fold and 100-fold increases, respectively, compared to naive mice. IL-4 was moderately enhanced in CHIT and CHIT-LA NP-vaccinated mice, showing a 10-fold and 16-fold increase, respectively (Fig. 11C). In the case of Th9, Th17, Th22, and Treg responses, only mice vaccinated with CHIT-MAN NPs showed a significant elevation in IL-17A and IL-22 levels, increasing by 300-fold and 45-fold, respectively, compared to unvaccinated controls (Fig. 11D). These results highlight that the mannosylated NPs triggered a broader and more robust immune response than the galactosylated or unmodified

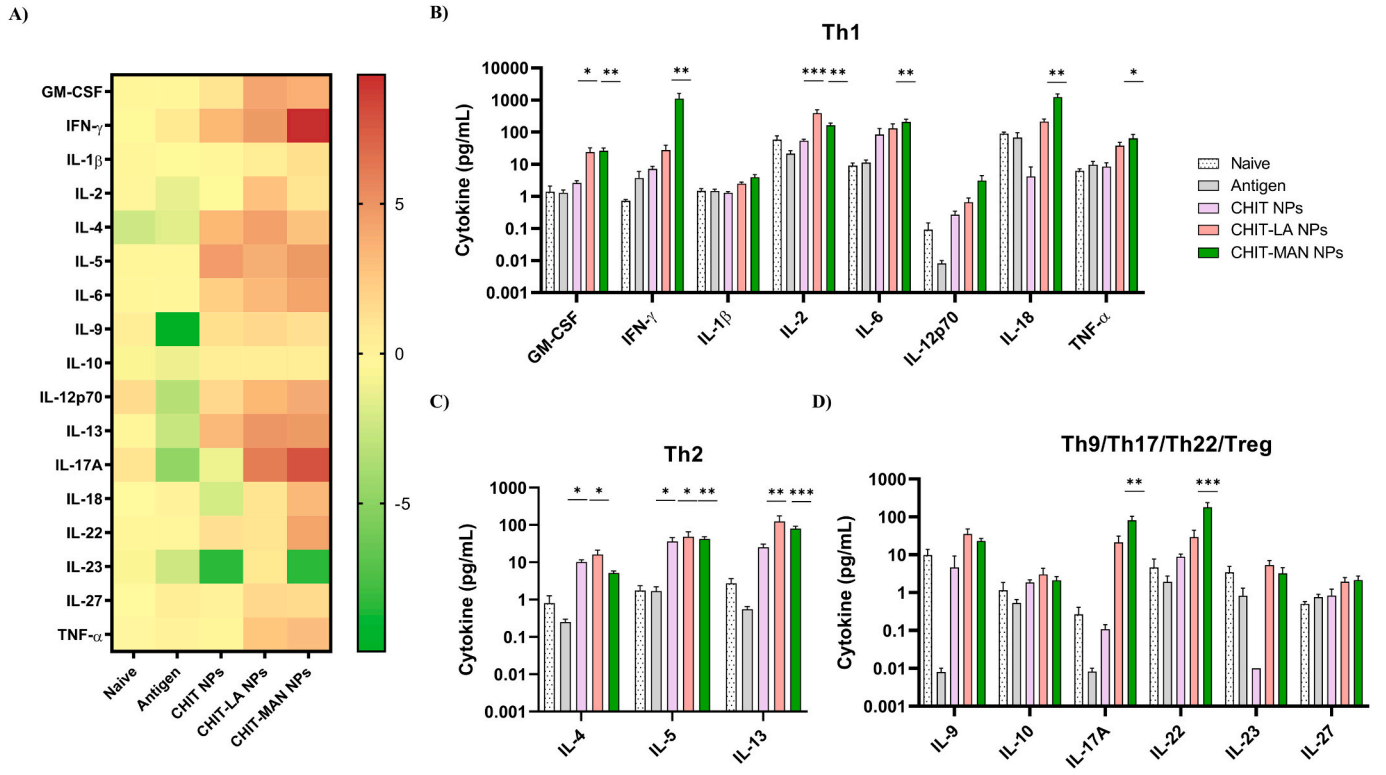


Fig. 11. Cytokine production in spleen cells following vaccination with chitosan-based protein-subunit vaccines after SARS-CoV-2 peptide restimulation. (A) A heatmap showing relative cytokine levels in spleen cell supernatants collected after 96 h of stimulation with 1 μg/mL of SARS-CoV-2 S protein peptides. The data are presented as the log2 fold change relative to the negative control group (spleen cells from naive mice also restimulated with peptides), with color intensities reflecting variations in cytokine concentrations. Each row represents a specific cytokine, while columns correspond to different vaccinated groups, with median values displayed for each condition. Cytokines linked to Th1 responses (B), Th2 responses (C) and Th9, Th17, Th22, and Treg pathways (D) were quantified in the supernatants (pg/mL) to provide a detailed quantitative assessment of immune polarization. Statistical analysis was conducted using the Kruskal-Wallis test followed by Dunn's multiple comparisons test with Bonferroni correction, and significant differences compared to the naive group are indicated as $*p < 0.05$, $**p < 0.01$, and $***p < 0.001$.

formulations in the spleen, a key systemic site of immune activation.

Lymphocytes isolated from lung tissue underwent a comparable analytical assessment, revealing an immune response profile consistent with that observed in splenic lymphocytes. Notably, the Th17 response in lung-derived lymphocytes was more extensive, with a wider array of Th17-associated cytokines detected. In contrast, the Th1 and Th2 responses closely mirrored those seen in splenic cells, showing no significant differences in their overall patterns (Fig. 12A). Specifically, regarding the Th1 response, only mice vaccinated with CHIT-MAN NPs demonstrated significant increases in GM-CSF, IL-1β, IL-6, IL-18, and TNF-α, with fold increases of 60, 21, 16, 4, and 7, respectively, compared to naive mice (Fig. 12B). In comparison, the CHIT-LA NPs elicited a more modest Th1 response in the lungs, with GM-CSF, IL-1β, IL-6, and IL-18 showing an upward trend; however, these changes were not statistically significant relative to unvaccinated mice. For the Th2 response, IL-5 was markedly elevated in mice vaccinated with CHIT-MAN NPs, reaching nearly 5000 pg/mL, compared to only 475 pg/mL in naive mice (Fig. 12C). Both CHIT-MAN and CHIT-LA NPs also induced IL-13 production, with 10-fold and 7-fold increases, respectively, compared to unvaccinated controls. Regarding the Th9/Th17/Th22/Treg, differences between the spleen and the lungs were anticipated due to the distinct immune environments of systemic *versus* mucosal tissues, especially following intranasal immunization. While the spleen primarily showed increases in IL-17A and IL-22 in mice vaccinated with CHIT-MAN NPs, the lung response was broader, with elevated levels of IL-9, IL-10, IL-23, and IL-27, in addition to IL-17A and IL-22 (Fig. 12D). This broader Th17 response highlights the need for a finely tuned balance between pro-inflammatory and regulatory pathways in mucosal tissues. IL-9, a cytokine linked to Th9 cells, contributes to epithelial barrier protection and enhances mast cell activity, aiding in pathogen clearance at the site of infection. IL-10, a critical regulatory cytokine, tempers excessive inflammation by limiting Th17 activity and suppressing the overproduction of pro-inflammatory mediators, thereby preventing tissue damage. IL-23, on the other hand, supports the expansion and maintenance of Th17 cells, ensuring their sustained activity to combat persistent pathogens [60]. IL-27 plays a dual role in the lung, initially amplifying Th1 and Th17 responses while later acting as a regulatory cytokine to dampen excessive inflammation. Together with IL-10, IL-27 creates a regulatory framework that modulates the activity of IL-17A and IL-22, ensuring a robust yet controlled immune defense in the respiratory tract [61].

Overall, the findings suggest that functionalizing chitosan NPs with mannose and gluconic acid enhances immune activation, particularly by promoting a diverse array of cytokines across multiple Th subsets. Notably, the MR has been widely recognized in literature as a critical target for amplifying vaccine responses, due to its ability to mediate antigen uptake and presentation by DCs and macrophages. The addition of gluconic acid to the formulation represents an innovative step, providing further stabilization to the NPs and enhancing their immunogenicity. These results highlight the potential of CHIT-MAN NPs to elicit a broad immune response and support their further investigation as a candidate platform for intranasal vaccination. Importantly, the present *in vivo* evaluation was performed at a single antigen dose; therefore, future dose-response studies will be needed to determine whether the antigen dose can be reduced while maintaining the observed immune responses.

Several protein subunit vaccines for SARS-CoV-2 have been developed and are approved for parenteral administration. For instance,

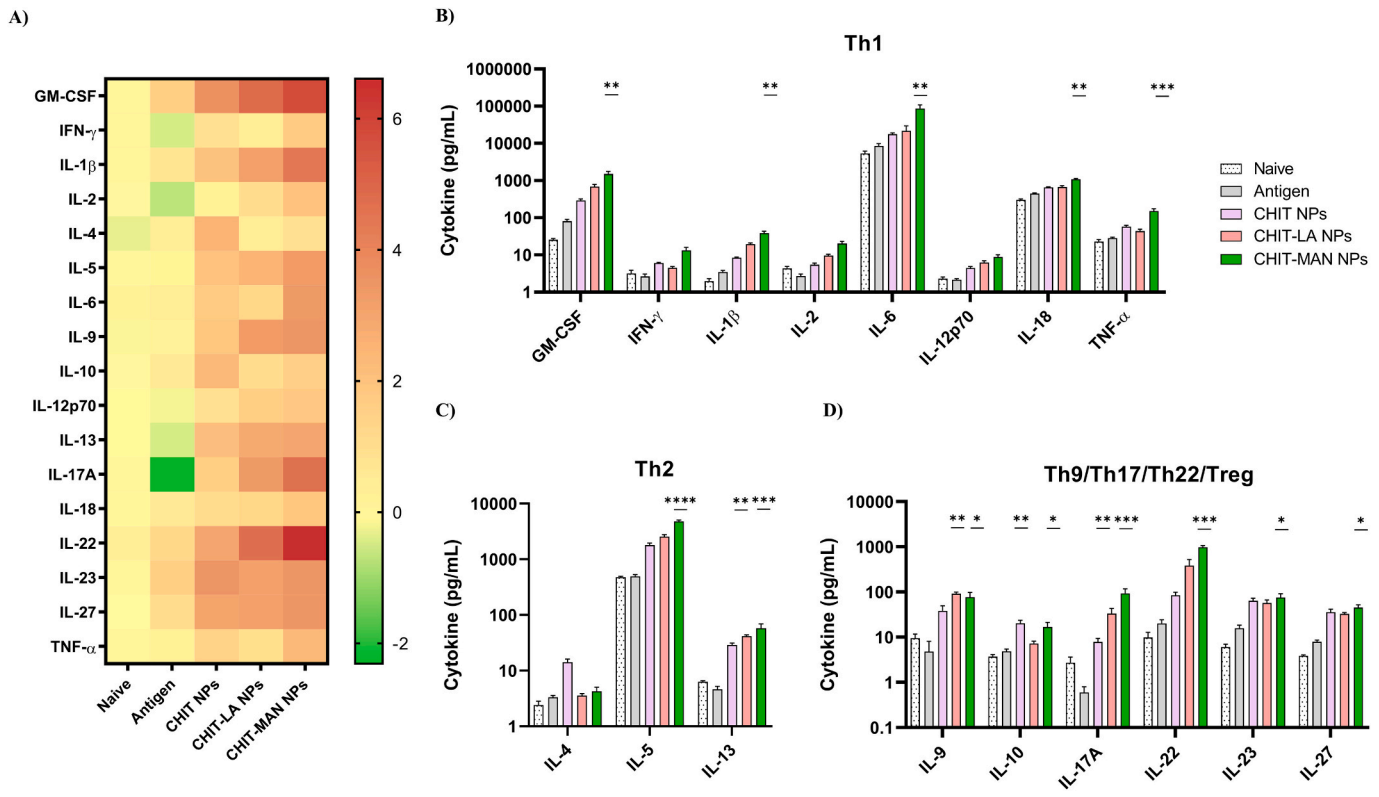


Fig. 12. Cytokine production in lung cells following vaccination with chitosan-based protein-subunit vaccines after SARS-CoV-2 peptide restimulation. (A) A heatmap showing relative cytokine levels in lung cell supernatants collected after 96 h of stimulation with 1 μg/mL of SARS-CoV-2 S protein peptides. The data are presented as the log2 fold change relative to the negative control group (lung cells from naive mice also restimulated with peptides), with color intensities reflecting variations in cytokine concentrations. Each row represents a specific cytokine, while columns correspond to different vaccinated groups, with median values displayed for each condition. Cytokines linked to Th1 responses (B), Th2 responses (C) and Th9, Th17, Th22, and Treg pathways (D) were quantified in the supernatants (pg/mL) to provide a detailed quantitative assessment of immune polarization. Statistical analysis was conducted using the Kruskal-Wallis test followed by Dunn's multiple comparisons test with Bonferroni correction, and significant differences compared to the naive group are indicated as $*p < 0.05$, $**p < 0.01$, and $***p < 0.001$.

Novavax (NVX-CoV2373) incorporates the Matrix-M adjuvant to boost immune responses and has received Emergency Use Listing by the World Health Organization [62]. Similarly, Corbevax, which uses aluminum hydroxide gel and CpG1018 as adjuvants, has been authorized for emergency use and stands out for its cost-effectiveness and accessibility [63]. VidPrevtyn Beta, developed by Sanofi and GSK, is a recombinant protein subunit vaccine produced using a baculovirus expression system. It contains the S protein from the B.1.351 variant of SARS-CoV-2 and is designed to enhance immune response with the inclusion of GSK's AS03 adjuvant, composed of squalene, polysorbate 80, and DL-α-tocopherol [64]. Other vaccines, such as Zifivax (ZF2001), Soberana® 02, and SpikoGen (COVAX-19), utilize a variety of adjuvants, including aluminum hydroxide [65], *tetanus toxoid* [66], and Advax-CpG [67], respectively. However, these vaccines are still awaiting broader regulatory approvals or have been authorized in limited regions. In contrast, Razi Cov Pars is the only protein subunit vaccine that includes an intranasal dose as part of its vaccination regimen. However, the intranasal administration is not evaluated as a standalone option; it is part of a layered vaccination strategy, following two intramuscular doses with the same adjuvant system [68]. This approach aims to stimulate both systemic and mucosal immune responses, but it also introduces logistical challenges and limits the vaccine's practicality as a purely mucosal option.

Parenteral vaccine delivery typically targets muscle tissue, which has fewer APCs compared to lymphoid and mucosal tissues. As a result, immune cell migration to the injection site often relies on injury-induced inflammation, which can influence the efficiency of the immune response. These constraints underscore the need for alternative vaccination strategies, particularly in the context of SARS-CoV-2, where mucosal immunity plays a crucial role in blocking respiratory infections. Our research addresses this gap by developing an intranasal protein-subunit SARS-CoV-2 vaccine that directly targets APCs at the site of administration. Unlike current vaccine platforms, our formulations use carbohydrate-modified polymers to enhance the safe and efficient delivery of antigens. This novel approach aims to overcome the limitations of traditional protein-subunit vaccines, providing a more effective and less invasive alternative to current market offerings.

4. Conclusion

The continued emergence of highly transmissible respiratory pathogens highlights the need for vaccination strategies capable of inducing robust mucosal immunity at the point of pathogen entry.

In this work, we explored three prototype chitosan-based NPs designed for the intranasal delivery of antigens as a prophylactic vaccine against SARS-CoV-2. Particular attention was given to the structure, surface properties and composition of the NPs. Functionalization of chitosan with sugar moieties, specifically lactobionic acid (CHIT-LA NPs) and gluconic acid/mannose (CHIT-MAN NPs), was performed to enhance receptor-mediated uptake in nasal tissues. These modifications preserved the core physicochemical properties of chitosan, including its mucoadhesive properties, while introducing receptor-specific interactions that facilitated enhanced permeation and uptake *via* receptor-mediated mechanisms. Among the nanoparticulate adjuvants studied, the combination of chitosan with gluconic acid and mannose showed pronounced biological responses across several endpoints, likely due to

the enhanced pro-inflammatory signaling capacity of the MR when compared to MGL targeted by lactobionic acid or the nonspecific targeting of unmodified chitosan. This enhanced signaling capacity was associated with macrophage activation characterized by prominent pro-inflammatory/M1-like features, including increased ROS and NO production and enhanced expression of M1-associated markers and inflammatory chemokines. *In vivo*, intranasal administration of the mannosylated NPs elicited marked cellular and humoral immune responses, including a balanced Th1/Th2/Th17 response and elevated antigen-specific sIgA production in mucosal secretions, underscoring their potential to provide both systemic and mucosal protection against SARS-CoV-2.

By targeting APCs at the pathogen entry point, intranasal vaccines can evoke localized immune responses that augment systemic immunity. This strategy holds promise not only for SARS-CoV-2 but also for other respiratory pathogens, such as influenza virus, respiratory syncytial virus, *Haemophilus influenzae* and *Streptococcus pneumoniae*. Moreover, this accessible administration route does not require specialized staff for immunization, making it particularly well-suited for global implementation, particularly in areas with limited resources. In summary, this study highlights the transformative potential of sugar-functionalized chitosan NPs as a next-generation platform for intranasal vaccination. The findings presented here lay the conceptual foundation for the development and regulatory approval of innovative, effective, and scalable vaccination strategies, addressing both current and future public health challenges.

CRediT authorship contribution statement

Mariana Colaço: Writing – review & editing, Writing – original draft, Methodology, Investigation, Formal analysis, Data curation, Conceptualization. **João Panão-Costa:** Writing – review & editing, Methodology, Investigation. **Elena Del Favero:** Visualization, Resources, Methodology, Formal analysis. **Caterina Ricci:** Visualization, Methodology, Formal analysis. **Virginia Patterlini:** Investigation, Conceptualization. **Giulia Climani:** Investigation, Conceptualization. **Ilaria Ferraboschi:** Visualization, Formal analysis. **Cristina Sissa:** Writing – review & editing, Validation, Resources. **Filipa Lebre:** Writing – review & editing, Validation, Formal analysis, Data curation. **Ernesto Alfaro-Moreno:** Validation, Resources, Project administration, Funding acquisition. **Fabio Sonvico:** Writing – review & editing, Validation, Supervision, Resources, Methodology. **Olga Borges:** Writing – review & editing, Supervision, Project administration, Funding acquisition, Conceptualization.

Informed consent statement

Informed consent was obtained from all subjects involved in the study for the PBMCs isolation.

Institutional review board statement

The study was conducted in accordance with the Declaration of Helsinki, and the protocol was approved by the Ethics Committee of the Faculty of Medicine, University of Coimbra, Portugal (approval number: 063-CE-2019; date of approval: 24 June 2019).

Declaration of competing interest

Mariana Colaço, João Panão-Costa and Olga Borges are co-inventors on a pending international Patent Cooperation Treaty (PCT) application entitled "Vaccine Adjuvants with Mucoadhesive Properties for Enhanced Immunogenicity Across a Spectrum of Diseases" (PCT/IB2025/061410), filed on 07 November 2025, which relates to part of the work reported in this manuscript. The other authors declare no competing interests.

Acknowledgments

This work was co-funded by the European Regional Development Fund (ERDF), through the Centro 2030 Regional Operational Programme under project CENTRO2030-FEDER-02604300, and through the COMPETE 2030 – Innovation and Digital Transition Operational Programme, and by the EU Recovery and Resilience Facility and Portuguese national funds *via* FCT – Fundação para a Ciência e a Tecnologia, under projects, LA/P/0058/2020 [DOI: 10.54499/LA/P/0058/2020], UID/PRR/4539/2025 [DOI: 10.54499/UID/PRR/04539/2025], UID/PRR2/4539/2025 [DOI: 10.54499/UID/PRR2/04539/2025], UID/04539/2025, 2023.16670.ICDT [DOI: 10.54499/2023.16670.ICDT], doctoral grant 2020.10043.BD and also *via* the 2021 edition of the Gilead GÉNESE Program (No. 13824). International Iberian Nanotechnology Laboratory research was funded by the European Union's H2020 project Sinfonia (No. 857253) and SbDToolBox (NORTE-01-0145-FEDER-000047), supported by Norte Portugal Regional Operational Programme (NORTE2020), under the PORTUGAL 2020 Partnership Agreement, through the ERDF. We also thank Professor Carla Vitorino, from the Faculty of Pharmacy, University of Coimbra, for providing access to her BioRender Academic Publication License, which was used to create the graphical abstract.

Appendix A. Supplementary data

Supplementary data to this article can be found online at https://doi.org/10.1016/j.ijbiomac.2026.154646.

Data availability

Data will be made available on request.

References

[1] S. Winklmeier, et al., Intramuscular vaccination against SARS-CoV-2 transiently induces neutralizing IgG rather than IgA in the saliva, Front. Immunol. 15 (2024), https://doi.org/10.3389/fimmu.2024.1330864.
[2] R. Koolaparambil Mukesh, et al., Intranasal booster induces durable mucosal immunity against SARS-CoV-2 in mice, Sci. Rep. 15 (1) (2025), https://doi.org/10.1038/s41598-025-06880-3.
[3] H.Y. Wu, H.H. Nguyen, M.W. Russell, Nasal lymphoid tissue (NALT) as a mucosal immune inductive site, Scand. J. Immunol. 46 (5) (2003) 506–513, https://doi.org/10.1046/j.1365-3083.1997.d01-159.x.
[4] B. Ying, et al., Mucosal vaccine-induced cross-reactive CD8+ T cells protect against SARS-CoV-2 XBB.1.5 respiratory tract infection, Nat. Immunol. 25 (3) (2024) 537–551, https://doi.org/10.1038/s41590-024-01743-x.
[5] D. Botta, et al., Intranasal immunization with live-attenuated RSV-vectored SARS-CoV-2 vaccines elicits antigen-specific systemic and mucosal immunity and protects against viral challenge and natural infection, Vaccines 14 (5) (2026) 399, https://doi.org/10.3390/vaccines14050399.
[6] H. Lei, et al., Intranasal delivery of a subunit protein vaccine provides protective immunity against JN.1 and XBB-lineage variants, Signal Transduct. Target. Ther. 9 (1) (2024), https://doi.org/10.1038/s41392-024-02025-6.
[7] K. Wørzner, et al., Intranasal recombinant protein subunit vaccine targeting TLR3 induces respiratory tract IgA and CD8 T cell responses and protects against respiratory virus infection, eBioMedicine 113 (2025) 105615, https://doi.org/10.1016/j.ebiom.2025.105615.
[8] S. Naskar, S. Sharma, K. Kuotsu, Chitosan-based nanoparticles: an overview of biomedical applications and its preparation, J. Drug Delivery Sci. Technol. 49 (2019) 66–81, https://doi.org/10.1016/j.jddst.2018.10.022.
[9] R.L. Atmar, et al., Norovirus vaccine against experimental human Norwalk virus illness, N. Engl. J. Med. 365 (23) (2011) 2178–2187, https://doi.org/10.1056/NEJMoa1101245.
[10] C.L. Bueter, et al., Spectrum and mechanisms of inflammasome activation by chitosan, J. Immunol. 192 (12) (2014) 5943–5951, https://doi.org/10.4049/jimmunol.1301695.
[11] M. Colaço, et al., Mannose and lactobionic acid in nasal vaccination: enhancing antigen delivery via C-type lectin receptors, Pharmaceutics 16 (10) (2024) 1308, https://doi.org/10.3390/pharmaceutics16101308.
[12] S. Jesus, et al., Chitosan nanoparticles: shedding light on immunotoxicity and hemocompatibility, Front. Bioeng. Biotechnol. 8 (2020), https://doi.org/10.3389/fbioe.2020.00100.
[13] J. S, Freeze dried chitosan/poly-ε-caprolactone and poly-ε-caprolactone nanoparticles: evaluation of their potential as DNA and antigen delivery systems, J. Genet. Syndr. Gene Ther. 4 (7) (2013), https://doi.org/10.4172/2157-7412.1000164.

[14] J. Castile, et al., Development of in vitro models to demonstrate the ability of PecSys®, an in situ nasal gelling technology, to reduce nasal run-off and drip, Drug Dev. Ind. Pharm. 39 (5) (2013) 816–824, https://doi.org/10.3109/03639045.2012.707210.
[15] M. Pozzoli, et al., Application of RPMI 2650 nasal cell model to a 3D printed apparatus for the testing of drug deposition and permeation of nasal products, Eur. J. Pharm. Biopharm. 107 (2016) 223–233, https://doi.org/10.1016/j.ejpb.2016.07.010.
[16] M. Colaço, et al., Intranasal administration of a DNA vaccine complexed with sugar-functionalized chitosan induces protective immunity against SARS-CoV-2 in mice, Int. J. Pharm. 700 (2026) 127048, https://doi.org/10.1016/j.ijpharm.2026.127048.
[17] D. Miteva, et al., Mucosal COVID-19 vaccines: risks, benefits and control of the pandemic, World J. Virol. 11 (5) (2022) 221–236, https://doi.org/10.5501/wjv.v11.i5.221.
[18] P. Félix, et al., Exploring TLR agonists as adjuvants for COVID-19 oral vaccines, Vaccine 53 (2025) 127078, https://doi.org/10.1016/j.vaccine.2025.127078.
[19] M. Colaço, et al., Optimizing mucosal vaccination: exploiting Lactobionic acid-modified chitosan for superior gene delivery systems, Int. J. Biol. Macromol. 327 (2025) 147492, https://doi.org/10.1016/j.ijbiomac.2025.147492.
[20] M. Colaço, et al., Dual functionalization of chitosan/DNA complexes with mannose and hydroxyl-rich acids for enhanced gene delivery efficiency, Int. J. Biol. Macromol. 357 (2026) 151595, https://doi.org/10.1016/j.ijbiomac.2026.151595.
[21] T.L. Moore, et al., Nanoparticle colloidal stability in cell culture media and impact on cellular interactions, Chem. Soc. Rev. 44 (17) (2015) 6287–6305, https://doi.org/10.1039/c4cs00487f.
[22] H. Heinz, et al., Nanoparticle decoration with surfactants: molecular interactions, assembly, and applications, Surf. Sci. Rep. 72 (1) (2017) 1–58, https://doi.org/10.1016/j.surfrep.2017.02.001.
[23] C. Prego, et al., Chitosan-based nanoparticles for improving immunization against hepatitis B infection, Vaccine 28 (14) (2010) 2607–2614, https://doi.org/10.1016/j.vaccine.2010.01.011.
[24] E. Soares, S. Jesus, O. Borges, Chitosan: β-glucan particles as a new adjuvant for the hepatitis B antigen, Eur. J. Pharm. Biopharm. 131 (2018) 33–43, https://doi.org/10.1016/j.ejpb.2018.07.018.
[25] E. Canelli, et al., Nano-adjuvanted dry powder vaccine for the mucosal immunization against airways pathogens, Front. Vet. Sci. 10 (2023), https://doi.org/10.3389/fvets.2023.1116722.
[26] M.E. Pereira, N.P. Macri, D.M. Creasy, Evaluation of the rabbit nasal cavity in inhalation studies and a comparison with other common laboratory species and man, Toxicol. Pathol. 39 (5) (2011) 893–900, https://doi.org/10.1177/0192623311409594.
[27] A. Giuliani, et al., In vivo nose-to-brain delivery of the hydrophilic antiviral ribavirin by microparticle agglomerates, Drug Deliv. 25 (1) (2018) 376–387, https://doi.org/10.1080/10717544.2018.1428242.
[28] S. Ejaz, et al., Surface engineering of chitosan nanosystems and the impact of functionalized groups on the permeability of model drug across intestinal tissue, Int. J. Biol. Macromol. 242 (2023) 124777, https://doi.org/10.1016/j.ijbiomac.2023.124777.
[29] F.A. Bruinsmann, et al., Chitosan-coated nanoparticles: effect of chitosan molecular weight on nasal transmucosal delivery, Pharmaceutics 11 (2) (2019) 86, https://doi.org/10.3390/pharmaceutics11020086.
[30] S. Bai, et al., Evaluation of human nasal RPMI 2650 cells grown at an air–liquid interface as a model for nasal drug transport studies, J. Pharm. Sci. 97 (3) (2008) 1165–1178, https://doi.org/10.1002/jps.21031.
[31] S. Höbel, et al., Maltose- and maltotriose-modified, hyperbranched poly(ethylene imine)s (OM-PEIs): physicochemical and biological properties of DNA and siRNA complexes, J. Control. Release 149 (2) (2011) 146–158, https://doi.org/10.1016/j.jconrel.2010.10.008.
[32] S. Ejaz, et al., Mannose functionalized chitosan nanosystems for enhanced antimicrobial activity against multidrug resistant pathogens, Polym. Test. 91 (2020) 106814, https://doi.org/10.1016/j.polymertesting.2020.106814.
[33] J.M. Calderon Moreno, M. Chelu, M. Popa, Eco-friendly bioinspired synthesis and environmental applications of zinc oxide nanoparticles mediated by natural polysaccharide gums: a sustainable approach to nanomaterials fabrication, Nanomaterials 16 (7) (2026) 407, https://doi.org/10.3390/nano16070407.
[34] S. Ejaz, et al., Add sugar to chitosan: mucoadhesion and in vitro intestinal permeability of mannosylated chitosan nanocarriers, Pharmaceutics 14 (4) (2022) 830, https://doi.org/10.3390/pharmaceutics14040830.
[35] X. Yang, et al., Permeation enhancer decorated nanoparticles for oral delivery of insulin: manipulating the surface density of borneol and PEG for absorption barriers, Biomater. Sci. (2025), https://doi.org/10.1039/d4bm01210k.
[36] A. Sadeghi, et al., Permeation enhancer effect of chitosan and chitosan derivatives: comparison of formulations as soluble polymers and nanoparticulate systems on insulin absorption in Caco-2 cells, Eur. J. Pharm. Biopharm. 70 (1) (2008) 270–278, https://doi.org/10.1016/j.ejpb.2008.03.004.
[37] I. Morshedi, et al., Smart nanoparticle vaccines integrate nanotechnology artificial intelligence and immunoengineering for precision immunization, Discov. Nano 21 (1) (2026), https://doi.org/10.1186/s11671-026-04656-w.
[38] A.W.S. de Souza, et al., M2 macrophage is the predominant phenotype in airways inflammatory lesions in patients with granulomatosis with polyangiitis, Arthritis Res. Ther. 19 (1) (2017), https://doi.org/10.1186/s13075-017-1310-4.
[39] S. Furgiuele, et al., Dealing with macrophage plasticity to address therapeutic challenges in head and neck cancers, Int. J. Mol. Sci. 23 (12) (2022) 6385, https://doi.org/10.3390/ijms23126385.
[40] D.A. Chistiakov, et al., CD68/macrosialin: not just a histochemical marker, Lab. Investig. 97 (1) (2017) 4–13, https://doi.org/10.1038/labinvest.2016.116.
[41] L. Su, et al., Glycocalyx-mimicking nanoparticles for stimulation and polarization of macrophages via specific interactions, Small 11 (33) (2015) 4191–4200, https://doi.org/10.1002/smll.201403838.
[42] L. Pinheiro do Nascimento, et al., Mannosylation of budesonide palmitate nanoprodrugs for improved macrophage targeting, Eur. J. Pharm. Biopharm. 170 (2022) 112–120, https://doi.org/10.1016/j.ejpb.2021.12.001.
[43] J. Ye, et al., Drug-free mannosylated liposomes inhibit tumor growth by promoting the polarization of tumor-associated macrophages, Int. J. Nanomedicine 14 (2019) 3203–3220, https://doi.org/10.2147/ijn.s207589.
[44] F. Wu, et al., Galactosylated LDL nanoparticles: a novel targeting delivery system to deliver antigen to macrophages and enhance antigen specific T cell responses, Mol. Pharm. 6 (5) (2009) 1506–1517, https://doi.org/10.1021/mp900081y.
[45] A. Sadeghi, et al., Curcumin ameliorates palmitate-induced inflammation in skeletal muscle cells by regulating JNK/NF-kB pathway and ROS production, Inflammopharmacology 26 (5) (2018) 1265–1272, https://doi.org/10.1007/s10787-018-0466-0.
[46] J. Checa, J.M. Aran, Reactive oxygen species: drivers of physiological and pathological processes, J. Inflamm. Res. 13 (2020) 1057–1073, https://doi.org/10.2147/jir.s275595.
[47] N. Takheaw, et al., Correlation analysis of anti-SARS-CoV-2 RBD IgG and neutralizing antibody against SARS-CoV-2 omicron variants after vaccination, Diagnostics 12 (6) (2022) 1315, https://doi.org/10.3390/diagnostics12061315.
[48] S. Feng, et al., Correlates of protection against symptomatic and asymptomatic SARS-CoV-2 infection, Nat. Med. 27 (11) (2021) 2032–2040, https://doi.org/10.1038/s41591-021-01540-1.
[49] F. Schmidt, et al., High genetic barrier to SARS-CoV-2 polyclonal neutralizing antibody escape, Nature 600 (7889) (2021) 512–516, https://doi.org/10.1038/s41586-021-04005-0.
[50] H. Takaki, et al., Mucosal immune response in nasal-associated lymphoid tissue upon intranasal administration by adjuvants, J. Innate Immun. 10 (5–6) (2018) 515–521, https://doi.org/10.1159/000489405.
[51] A. Debin, et al., Intranasal immunization with recombinant antigens associated with new cationic particles induces strong mucosal as well as systemic antibody and CTL responses, Vaccine 20 (21−22) (2002) 2752–2763, https://doi.org/10.1016/s0264-410x(02)00191-3.
[52] S.H. Soh, et al., Induction of Th2-related immune responses and production of systemic IgA in mice intranasally immunized with Brucella abortus malate dehydrogenase loaded chitosan nanoparticles, Vaccine 37 (12) (2019) 1554–1564, https://doi.org/10.1016/j.vaccine.2019.02.005.
[53] D. Pawar, K.S. Jaganathan, Mucoadhesive glycol chitosan nanoparticles for intranasal delivery of hepatitis B vaccine: enhancement of mucosal and systemic immune response, Drug Deliv. 23 (1) (2014) 185–194, https://doi.org/10.3109/10717544.2014.908427.
[54] H. Jiang, et al., Preparation and characterization of curdlan-chitosan conjugate nanoparticles as mucosal adjuvants for intranasal influenza H1N1 subunit vaccine, Int. J. Biol. Macromol. 266 (2024) 131289, https://doi.org/10.1016/j.ijbiomac.2024.131289.
[55] Z. Sadeghi, et al., Mannosylated chitosan nanoparticles loaded with FliC antigen as a novel vaccine candidate against Brucella melitensis and Brucella abortus infection, J. Biotechnol. 310 (2020) 89–96, https://doi.org/10.1016/j.jbiotec.2020.01.016.
[56] Y. Gong, et al., Enhancing cell-mediated immunity through dendritic cell activation: the role of Tri-GalNAc-modified PLGA-PEG nanoparticles encapsulating SR717, Front. Immunol. 15 (2024), https://doi.org/10.3389/fimmu.2024.1490003.
[57] B. Lou, et al., Modular core-shell polymeric nanoparticles mimicking viral structures for vaccination, J. Control. Release 293 (2019) 48–62, https://doi.org/10.1016/j.jconrel.2018.11.006.
[58] Y. Du, et al., Engineering mannosylated pickering emulsions for the targeted delivery of multicomponent vaccines, Biomaterials 280 (2022) 121313, https://doi.org/10.1016/j.biomaterials.2021.121313.
[59] T. Arshad, et al., A double edged sword role of interleukin-22 in wound healing and tissue regeneration, Front. Immunol. 11 (2020), https://doi.org/10.3389/fimmu.2020.02148.
[60] G.L. Stritesky, N. Yeh, M.H. Kaplan, IL-23 promotes maintenance but not commitment to the Th17 lineage, J. Immunol. 181 (9) (2008) 5948–5955, https://doi.org/10.4049/jimmunol.181.9.5948.
[61] C.B. Lopez, et al., Early IL-6 signalling promotes IL-27 dependent maturation of regulatory T cells in the lungs and resolution of viral immunopathology, PLoS Pathog. 13 (9) (2017) e1006640, https://doi.org/10.1371/journal.ppat.1006640.
[62] D.V. Parums, Editorial: first approval of the protein-based adjuvanted Nuvaxovid (NVX-CoV2373) Novavax vaccine for SARS-CoV-2 could increase vaccine uptake and provide immune protection from viral variants, Med. Sci. Monit. 28 (2022), https://doi.org/10.12659/msm.936523.
[63] S. Thuluva, et al., Evaluation of safety and immunogenicity of receptor-binding domain-based COVID-19 vaccine (Corbevax) to select the optimum formulation in open-label, multicentre, and randomised phase-1/2 and phase-2 clinical trials, eBioMedicine 83 (2022) 104217, https://doi.org/10.1016/j.ebiom.2022.104217.
[64] European Medicines Agency, EMA recommends approval of VidPrevtyn Beta as a COVID 19 booster vaccine, Available from: https://www.ema.europa.eu/en/news/ema-recommends-approval-vidprevtyn-beta-covid-19-booster-vaccine, 2022.
[65] V. Garib, et al., Milk of cow and goat, immunized by recombinant protein vaccine ZF-UZ-VAC2001(Zifivax), contains neutralizing antibodies against SARS-CoV-2

and remains active after standard milk pasteurization, Front. Nutr. 9 (2022), https://doi.org/10.3389/fnut.2022.901871.
[66] R. Pérez-Nicado, et al., Comparative immune response after vaccination with SOBERANA® 02 and SOBERANA® plus heterologous scheme and natural infection in young children, Vaccines 11 (11) (2023) 1636, https://doi.org/10.3390/vaccines11111636.
[67] L. Li, et al., Covax-19/Spikogen® vaccine based on recombinant spike protein extracellular domain with Advax-CpG55.2 adjuvant provides single dose protection against SARS-CoV-2 infection in hamsters, Vaccine 40 (23) (2022) 3182–3192, https://doi.org/10.1016/j.vaccine.2022.04.041.
[68] S.R. Banihashemi, et al., Safety and efficacy of combined intramuscular/intranasal RAZI-COV PARS vaccine candidate against SARS-CoV-2: a preclinical study in several animal models, Front. Immunol. 13 (2022), https://doi.org/10.3389/fimmu.2022.836745.